Testing gas dispersion modelling: A case study at La Soufrière volcano (Guadeloupe, Lesser Antilles)

Silvia Massaro [a,b,*], Fabio Dioguardi [c], Laura Sandri [a], Giancarlo Tamburello [a], Jacopo Selva [a], Séverine Moune [d,e,f], David E. Jessop [d,e,f], Roberto Moretti [d,e], Jean-Christophe Komorowski [d], Antonio Costa [a]

[a] Istituto Nazionale di Geofisica e Vulcanologia, Sezione di Bologna, Italia
[b] Istituto di Geologia Ambientale e Geoingegneria, Consiglio Nazionale delle Ricerche, Area di Ricerca Roma 1, Sede Montelibretti, Italia
[c] British Geological Survey, The Lyell Centre, Edinburgh, United Kingdom
[d] Université de Paris, Institut de Physique du Globe de Paris, UMR CNRS 7154, Paris, France
[e] Observatoire Volcanologique et Sismologique de Guadeloupe, Institut de Physique du Globe de Paris, Gourbeyre, Guadeloupe
[f] Université Clermont Auvergne, CNRS, IRD, OPGC Laboratoire Magmas et Volcans, F-63000 Clermont-Ferrand, France

ARTICLE INFO

ABSTRACT

Volcanic gas dispersal can be a serious threat to people living near active volcanoes since it can have short- and long-term effects on human health, and severely damage crops and agricultural land. In recent decades, reliable computational models have significantly advanced, and now they may represent a valuable tool to make quantitative and testable predictions, supporting gas dispersal forecasting and hazard assessments for public safety. Before applying a specific modelling tool into hazard quantification, its calibration and its sensitivity to initial and boundary conditions should be carefully tested against available data, in order to produce unbiased hazard quantifications. In this study, we provided a number of prototypical tests aimed to validate the modelling of gas dispersal from a hazard perspective. The tests were carried out at La Soufrière de Guadeloupe volcano, one of the most active gas emitters in the Lesser Antilles.

La Soufrière de Guadeloupe has shown quasi-permanent degassing of a low-temperature hydrothermal nature since its last magmatic eruption in 1530 CE, when the current dome was emplaced. We focused on the distribution of CO_2 and H_2S discharged from the three main present-day fumarolic sources at the summit, using the measurements of continuous gas concentrations collected in the period March–April 2017. We developed a new probabilistic implementation of the Eulerian code DISGAS-2.0 for passive gas dispersion coupled with the mass-consistent Diagnostic Wind Model, using local wind measurements and atmospheric stability information from a local meteorological station and ERA5 reanalysis data. We found that model outputs were not significantly affected by the type of wind data but rather upon the relative positions of fumaroles and measurement stations. Our results reproduced the statistical variability in daily averages of observed data over the investigated period within acceptable ranges, indicating the potential usefulness of DISGAS-2.0 as a tool for reproducing the observed fumarolic degassing and for quantifying gas hazard at La Soufrière. The adopted testing procedure allows for an aware application of simulation tools for quantifying the hazard, and thus we think that this kind of testing should actually be the first logical step to be taken when applying a simulator to assess (gas) hazard in any other volcanic contexts.

1. Introduction

Volcanic gases are mixtures of volatile compounds generated by magmas exsolving volatiles at low pressures during their ascent and storage near the surface. The solubilities of volatile components demand that gas compositions are dominated by the more melt-soluble components (such as H_2O, SO_2 and halogens), with CO_2 solubility decreases as magma decompresses and ascends up to the surface. However, even for open-conduit-volcano, processes are more complicated than this simple sketch. On one hand, depending on the state of the volcano and its internal dynamics, volcanic gas compositions sum-up the degassing from shallow magma and the deeper portions of the plumbing system, down to the magma chamber (e.g., Symonds, 1994; Oppenheimer et al., 2011; Moretti et al., 2013; Aiuppa et al., 2007, 2010, 2016, 2017a; Erfurt-Cooper, 2018). On the other hand, at closed-conduit and generally andesitic volcanoes, we observe focused vents (fumaroles) releasing in atmosphere steam-rich (>90% vol; e.g., Giggenbach, 1996) compositions that reflect the sharp physico-chemical change from the

magma resident in the crust towards the shallower low-temperature and low-pressure environment dominated by brines and hot water rather than melts (e.g., Giggenbach, 1996; Moretti and Stefansson, 2020 and references therein).

Although the impacts from large volcanic eruptions on the global environment have been widely studied (e.g., Hofmann, 1987; Grattan and Pyatt, 1999; Parker et al., 1996; Oppenheimer, 2002; Self, 1845), those of lower tropospheric emissions from persistently degassing volcanoes still remain poorly known. On a time-averaged basis, gas emissions from persistent passive volcanic degassing greatly exceed those from sporadic eruptive activity (e.g., Andres and Kasgnoc, 1998; Oppenheimer et al., 2003), producing significant long-term (years to decades) effects at local and regional scales, both on humans and the environment (e.g., Tortini et al., 2017 and references therein).

The dispersion of gas denser than air released from a given source is governed by gravity and by dilution through mixing with ambient air from the plume margins, which decreases density. Close to the source, buoyancy controls the gas transport (e.g., Hankin and Britter, 1999; Costa et al., 2008; Folch et al., 2009), but when the density contrast becomes negligible, gas dispersion is basically governed by the wind and atmospheric turbulence (passive dispersion). In order to capture all the dispersion regimes, numerical models need to solve the complete 3D equations system for mass, momentum, and energy transport (e.g., Macedonio and Costa, 2002; Cortis and Oldenburg, 2009). However, in conditions of passive dispersion regime, simplifying assumptions can be made since gases are driven by wind advection and atmospheric turbulence, making the problem computationally easier (e.g., Costa et al., 2005; Costa and Macedonio, 2016).

Although the advances carried out in the past two decades (e.g., Scire et al., 2000; Stein et al., 2015; Folch et al., 2017), the evaluation of accurate location, magnitude and timing of ground-level concentrations is far from being achieved. Errors in predictions are introduced into results by the approximations associated with the physics and formulation used to model dispersion, and by the uncertainty on input parameters, such as source emission (e.g., Venkatram, 1981) and meteorological data (e.g., Lewellen and Sykes, 1989; Dabbert and Miller, 2000).

Since gas dispersal is controlled by local wind fields and atmospheric turbulence, the study of the short-lived phenomena smaller than mesoscale (i.e., micrometeorology) represents one of the most significant factors in determining the quality of results along with the suitability of the model and the availability of accurate information on the gas source (e.g., Boybeyi and Raman, 1995). However, the issues that determine whether or not models will provide more realistic results vary from case to case. As a starting point, validation studies are strictly required to provide some guidance on how to properly use these models to forecast gas dispersion and how to quantify the associated uncertainties.

In this study, we tested the capability of DISGAS-2.0 (Dispersion of GASes; Costa and Macedonio, 2016) to be applied in a hazard perspective, i.e., its ability in reproducing the correct order of magnitude and variability (e.g., Tierz et al., 2016) of gas concentrations dispersed from the summit dome fumaroles on La Soufrière de Guadeloupe (Fig. 1a-b), which is currently the second most active emitter of volcanic gases in the Lesser Antilles island arc, after Soufrière Hills in Montserrat. The volcano has been in unrest since 1992 and represents the most important volcanic hydrothermal system of the region whose present-day fumarolic activity is dominated by a passive dispersion regime.

Here, we aimed to reproduce the order of magnitude and variability in daily averages of CO_2 and H_2S concentrations on the main active fumaroles: i) Gouffre-56 (G56); ii) Tarissan (TAS); iii) Cratère Sud (CS) (Fig. 1). Taking into account Tamburello et al. (2019), we focussed on the time interval from 29/03/2017 to 10/04/2017, a period covered by continuous and simultaneous gas concentration measurements at these three sources. Since for this period there are no contemporary measurements of gas flux and composition at the sources, we used the

available gas flux data in literature (Allard et al., 2014; Tamburello et al., 2019) accounting for the related uncertainty. Additional uncertainty derives from used wind field due to the resolution of the Digital Elevation Model (DEM). This type of uncertainty, sometimes defined as "parametric" (e.g., Rougier and Beven, 2013; Tierz et al., 2017), was modelled by running DISGAS-2.0 on different wind models and/or DEMs, and stochastically varying the gas fluxes and molar ratios for each source. The goal of this study is to quantify how much the daily-average concentrations are affected by these uncertainties, and if the model suitably reproduces the statistics of the observations.

2. Geo-volcanological context and hydrothermal activity

La Soufrière de Guadeloupe (herein referred to as La Soufrière) is the most recent volcanic edifice belonging to the Grande Découverte volcanic complex built during the past 445 ka (Komorowski et al., 2005). Magma composition is very homogeneous and represented essentially by medium K-calc-alkaline basaltic andesites and andesites (Boudon et al., 2008; Pichavant et al., 2018). It is an active explosive volcano that experienced magmatic and non-magmatic phreatic eruptions in the past (Feuillard et al., 1983; Komorowski et al., 2005; Legendre, 2012; Moretti et al., 2020a). The present lava dome was emplaced about 500 years ago, following eight dome collapse events that occurred over the past 8500 years (Komorowski et al., 2005; Boudon et al., 2008), often caused by blasts of hydrothermal fluids expanding laterally at estimated speeds of 100–230 m s^{-1} (Feuillard et al., 1983; Villemant et al., 2014).

The coexistence of an active magma chamber and abundant groundwater fed by a tropical-climate rainfall regime (7–10 m y^{-1} on the summit area; OVSG-IPGP Bilan mensuel de l'activité volcanique de la Soufrière de Guadeloupe et de la sismicité régionale, 1999–2013) has led to the formation of a well-developed hydrothermal system with persistent manifestations (i.e., fumaroles, solfataras, hot springs) at sites where heat is preferentially transported to the surface (Boichu et al., 2011; Ruziè et al., 2012; Gaudin et al., 2013; Brothelande et al., 2014; Villemant et al., 2014; Allard et al., 2014; Rosas-Carbajal et al., 2016; Tamburello et al., 2019; Moretti et al., 2020a, 2020b; Jessop et al., 2021), as commonly observed at many volcanoes in hydrothermal stage (e.g. Brombach et al., 2001; Chiodini et al., 2001; Hernàndez et al., 2012; Rissmann et al., 2012; Di Napoli et al., 2009; Moretti et al., 2018; Harris et al., 2013; Sigurdsson et al., 2015). The historical activity has been characterised by several intermittent non magmatic steam-driven phreatic eruptions (e.g., 1690, 1797–98, 1812, 1836–37, 1956 and 1976–77 CE, Komorowski et al., 2005). The last 1976–77 eruption was interpreted as a stillborn (or failed) magmatic eruption (e.g., Villemant et al., 2005; Boichu et al., 2008, 2011; Ruzié et al., 2012) where a small andesitic magma volume stopped its ascent approximately 3 km below the surface.

The historical temperature record shows that fumarolic vents typically have temperatures corresponding to saturated steam vapour at the pressure of the summit (95 °C), with short-lived fluctuations up to 140 °C during 1999–2000 (Moretti et al., 2020a). After the 1976–77 eruption, a decline of fumarolic activity was observed both on the summit and at the base of the lava dome until 1992, when a progressive increase of degassing occurred (Zlotnicki et al., 1992). Since 1996–97, activity has intensified at the summit (Komorowski et al., 2001, 2005; Fig. 1b), whilst flank activity has all but vanished (Zlotnicki et al., 1992; Moretti et al., 2020a; Jessop et al., 2021; OVSG-IPGP Bilan mensuel de l'activité volcanique de la Soufrière de Guadeloupe et de la sismicité régionale, 1999–2013).

More recently, fumarolic activity resumed at Gouffre-56 in 2007 (Fig. 1b) and new sources appeared in the summit area between 2011 and 2016 (Brothelande et al., 2014; Tamburello et al., 2019). This recent hydrothermal activity is compatible with an increasingly vapour-dominated system favourable to local destabilization, as shown by at least two small explosions that occurred in 2016 in the Napoléon Est
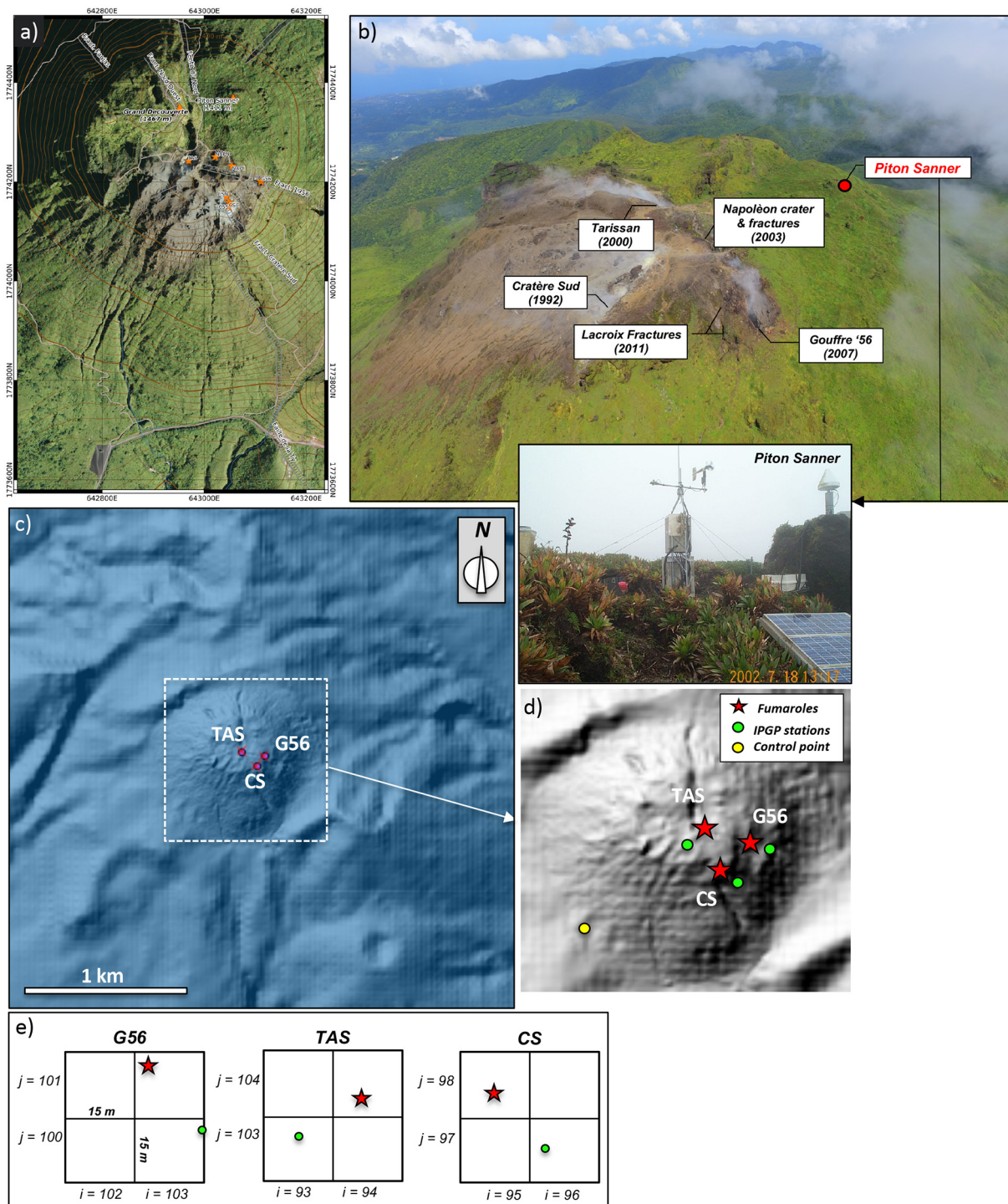
Fig. 1. a) Map of the summit La Soufrière de Guadeloupe volcano (1467 m asl) showing the main geological features (1956 fractures, Cratère Sud, Fente du Nord, Nord-Ovest, Faujas, and La Ty fault), the location of the active fumaroles (red stars) b) photo of the main active fumaroles (Cratère Sud, 1992; Gouffre-56, 2007; Napolèon crater and fractures, 2003; Tarissan, 2000; Lacroix fractures, 2011) modified from Moretti et al., (2020b) and Jessop et al. (2021), and the meteorological station Piton Sanner (1411 m asl); c) Computational domain (ca. 3 km × 3 km) used for numerical simulations. The grid used is set 200 × 200 (resolution = 15 m). The three investigated sources (Cratère Sud, CS; Tarissan, TAS; Gouffre-56, G56) are shown as pink dots; d) Magnification of the summit dome area where are shown the location of the fumarolic sources (red stars; G56: 643531 E, 1774515 N; TAS: 643396 E, 1774549 N; CS: 643481 E, 1774456 N), the IPGP measurement stations (green dots; G56: 643545 E, 1774499 N; TAS: 643388 E, 1774541 N; CS: 643489 E, 1774441 N) and the control point located at the south-western flank (yellow dot; 643,108 E; 1,774,190 N); e) Position of the fumarolic sources (red stars) and stations (tracking points, green dots) on the cells (i,j) of the 15 m-resolution computational grid.

(NAPE in Fig. 1a) vent (Le Gonidec et al., 2019). From 2012 to 2016, the total gas flux increased at CS and TAS vents, while at G56 varied from below detection limit to values that are comparable to the gas flux from TAS (e.g., Allard et al., 2014; Tamburello et al., 2019). Since 2016, measurements show constant gas fluxes at TAS and CS, with mean values of 5.7 ± 1.6 and 7.5 ± 1 t/d, respectively. Taking into account the high error (about 40%) on the flux determination (Tamburello et al., 2019; Jessop et al., 2021), the gas fluxes at G56 can be considered overall steady, despite a noticeable variability for short periods of time (4.7 ± 2.6 t/d; Moretti et al., 2020b).

In particular, a recent, complete inventory of the heat flux discharged by the dome (particularly its partitioning between fumarolic, soil diffuse and hot spring fluxes) has shown that, whereas fumarolic output from the main sources has slowly declined over the past decade, the emergence of new sites, the concurrent increase in soil temperature, and the extent of vegetation decay on the volcano has meant that the overall heat budget has increased from 29.8 MW to 36.5 MW between 2010 and 2020 (Jessop et al., 2021).

3. Methods

3.1. Gas measurements

Data acquisition at La Soufrière is often complicated by unstable weather (high rainfall rate, humidity commonly close to 100%; Allard et al., 2014). The summit of this volcano (1467 m above sea level) is the highest in the Lesser Antilles. As such, weather conditions can change rapidly: sunny intervals alternate with episodes of fog and occasional rain, and trade winds generally blowing from the northeast can vary suddenly in speed. Wind speed is a key parameter and its uncertainty is the main source of uncertainty in quantifying volcanic gas fluxes (McGonigle et al., 2002; Jessop et al., 2021), therefore the collection of gas concentrations and flux measurements under stable meteorological conditions are quite exceptional on top.

The Observatoire Volcanologique et Sismologique de la Guadeloupe and Institute de Physique du Globe de Paris (OVSG-IPGP) uses routinely the Multi-component Gas Analysing System (MultiGAS, Aiuppa et al., 2005; Shinohara, 2005) which is composed by a light and compact device with an infrared spectrometer and electrochemical sensors that allows simultaneous analysis of H_2O, CO_2, SO_2, H_2S and H_2 mixing ratios in air-diluted volcanic plumes. It is used for discrete measurements but also for permanent gas surveys that are currently operated on several volcanoes worldwide (e.g., de Moor et al., 2016; Aiuppa et al., 2007, 2010, 2017a, 2017b). Moretti et al. (2020b) evidenced the good match between on-site MultiGAS measurements and the analyses from direct sampling of low-temperature fumaroles, although some minor, but systematic, departures can be observed. The latter are related to secondary phenomena, such as gas scrubbing from water droplets in air and diffusive gradients in the MultiGAS sampling line imposed by the inlet filter and the pump.

Allard et al. (2014) and Tamburello et al. (2019) used portable MultiGAS to determined the fumarolic gas fluxes and compositions by walking transects perpendicular to the three main vents (CS, TAS, and G56; Fig. 1c). A derived integral of the total gas distributed along each plume cross-section (the integrated column amount) is then multiplied by the average wind speed (see Tamburello et al., 2019 for more details) to obtain the gas flux. Water vapour greatly prevails (~86–97%) in all gas mixtures emitted at above or near the water boiling temperature (96 °C) at ambient elevation, while CO_2 is the second most abundant component, followed by H_2S (Tamburello et al., 2019; Moretti et al., 2020a, 2020b).

Jessop et al. (2021) reported that some temporal variability of steam fluxes could be due to the different ambient humidity and weather condition at the summit between field measurements and occasional partial steam condensation on the external sensors. However, this condensed water is not taken into account by the MultiGAS measurements. It has been shown that, in such tropical conditions, properly accounting for the condensed water additionally adds approximately 40% to the steam flux estimations, an increase which we considered in our simulations.

Despite the fact that the derived CO_2 and H_2S fluxes are affected by these changing conditions, they can be considered as constant values at single vents on time scales of a few days, months and even years, if no change of magmatic conditions occur, despite variable waterfalls and although we are aware that changes in the water table could change them.

Proximal gas concentrations at each fumarolic site were recorded with the OVSG-IPGP network of permanent MultiGAS stations. These stations are located a few meters from each emission point (643,545 E; 1,774,499 N at G56, 643388 E; 1,774,541 N at TAS, and 643,489 E; 1,774,441 N at Cratère Sud, considering the UTM coordinate system, sector 20 N, Fig. 1a). Each station was equipped with an infra-red sensor for CO_2 (model Gascard NG, range 0–5000 ppmv, accuracy ±2%), two electrochemical sensors for H_2S and SO_2 (City Technology, sensor type T3ST/F for SO_2, range 0–50 ppmv, accuracy of ±2%, resolution 0.1 ppmv, and TC4F-1A for H_2S, range 0–100, accuracy of ±2%, resolution 0.1 ppmv). Each sensor was calibrated using standard gas mixtures in the laboratory of the local volcanic observatory (OVSG-IPGP) before installation. A Campbell Scientific CR6 data-logger followed a duty cycle schedule and recorded data at 1 Hz for a 20 min-long period every six hours, data were periodically transmitted to the OVSG. All sensors and data-logger were housed inside a water-proof aluminium box (33 × 23 × 18 cm), with the external volcanic gas-air mixture pumped at ~1.5 l/min by a membrane pump via silicon tubing and connected to 1 μm filter to prevent water entering inside the tubes. The gas inlet was placed at ~1 m height above the ground. The system was powered by a 12 V (~100 Ah) lithium battery stored in a polypropylene water-proof box (56 × 86 × 33 cm) together with the aluminium box. Acquisitions ran for 20 min every 6 h, apart for a few days for which the measurements were shorter (2 min) due to detection of low volcanic gas (H_2S concentration < 2 ppmv).

3.2. Numerical model

Atmospheric gas dispersion can be described by solving equations for the conservation of mass, momentum, and energy (the Navier-Stokes equations) in 3D, for each species of gas. However, in practice, several simplifications, which describe only specific phases or aspects of gas transport, are commonly used (e.g., Costa and Macedonio, 2016). Passive dispersion approach is used when the gas is diluted enough with respect to the surrounding atmosphere, and the validity of such an approximation can be assessed by estimating the Richardson number:

$$R_i = \frac{1}{v^2}\left(\frac{g'q}{R}\right)^{\frac{2}{3}} = \frac{\sqrt[3]{\frac{g^2(\rho_g-\rho_a)^2}{\rho_a^2}q^2}}{v^2R^{\frac{2}{3}}} \tag{1}$$

where g is the gravity acceleration, ρ_g and ρ_a are the air and the gas densities respectively, q is the volumetric flow rate, R the plume size (e.g., plume radius), and v is the wind velocity at the reference altitude (i.e., 10 m). For $R_i < 0.25$ transport is substantially passive whereas for $R_i > 1$ is mainly density driven (Cortis and Oldenburg, 2009; Costa et al., 2013). In our case, the passive condition at source is ensured since the fumaroles (mainly composed of H_2O, CO_2 and H_2S) have a mean gas density of ca. 0.54 kg m^{-3} at $T = 100$ °C, and $P = 900$ mbar, and the air density is ca. 1.03 kg m^{-3} (at $T = 18$ °C, P = 900 mbar). For instance, considering a maximum gas flow rate used in this work (0.043 m^3 s^{-1}; see Table 1) in calm wind conditions (0.5 m s^{-1}), for a plume size having a radius R of ca. 30 m, we have $R_i \approx 0.15$.

According to this approach, gas transport is off-line coupled with the output of the mass-consistent Diagnostic Wind Model (DWM; Douglas et al., 1990) for the wind field over a realistic topography model. The DWM generates wind components (u, v, w) at several user-specified vertical levels for a specified time, incorporating local surface and upper-air wind observations, where available, and providing some information on terrain-induced air flows in regions where local observations are absent. In particular, the generation of the wind field is obtained by a two-step procedure. Step l produces a spatially varying gridded field of wind components (u, v, w) for each vertical layer within the modelling domain. Step 2 combines the gridded wind field generated in step l with available observational data to produce a final

Table 1
H_2O fluxes (kg s^{-1}) sampled by the ECDF (Appendix B) for G56, TAS and CS sources. For each source, the flux values have been sampled once a day, for each of the 11 simulations. All the sampled fluxes have been increased by 40% in order to take into account the underestimation provided by MultiGAS.

Gouffre-56

G56	29/03/17	30/03/17	31/03/17	01/04/17	02/04/17	03/04/17	04/04/17	05/04/17	06/04/17	07/04/17	08/04/17	09/04/17	10/04/17
flux 0	1.778	0.6706	0.602	1.204	1.036	0.672	2.016	0.952	1.414	1.218	0.63	13.3	0.476
flux 1	0.35	20.51	0.7	1.68	0.6706	1.68	1.3566	1.0192	2.0664	0.7196	2.0664	0.7196	20.51
flux 2	0.9744	1.428	1.344	2.408	0.7686	2.408	0.9604	0.756	2.0272	0.532	0.6832	0.826	0.448
flux 3	0.7196	0.1078	0.364	0.826	1.2208	1.3636	0.63	0.91	27.3	0.3654	0.1078	1.4798	2.408
flux 4	0.7686	1.3566	2.1	0.924	0.707	0.875	0.35	0.6594	0.3654	43.33	2.408	1.0192	1.4182
flux 5	0.9604	0.756	0.714	21.7	0.3654	0.4844	31.92	0.875	0.756	2.0272	0.7686	0.448	0.6076
flux 6	1.0192	0.35	0.742	0.3654	1.0192	0.9352	1.4798	0.602	0.448	1.0192	1.092	0.742	0.9352
flux 7	0.0518	1.204	1.134	0.742	21.7	1.778	0.714	0.3654	21.7	0.6076	0.7196	0.7686	0.4256
flux 8	0.1078	21.7	1.428	0.756	0.7196	43.33	1.036	32.9	0.707	1.0472	0.3654	32.9	1.3566
flux 9	32.9	1.0472	1.47	0.4844	0.6076	0.924	0.3654	0.714	1.036	1.778	0.9912	0.91	1.2208
flux 10	3.99	0.63	1.0612	3.108	2.8826	5.446	4.074	3.976	5.782	5.264	0.9828	6.706	2.968

Tarissan

TAS	29/03/17	30/03/17	31/03/17	01/04/17	02/04/17	03/04/17	04/04/17	05/04/17	06/04/17	07/04/17	08/04/17	09/04/17	10/04/17
flux 0	0.6272	0.959	2.0664	0.4256	1.092	0.1078	1.778	0.6706	1.204	32.9	31.92	27.3	0.7672
flux 1	0.3654	0.7196	0.364	1.2908	0.714	0.3654	1.4798	0.448	0.756	1.036	32.9	1.2922	1.2922
flux 2	1.036	2.0664	0.35	0.6076	21.7	1.2922	0.868	1.204	2.0272	1.4798	1.428	0.9352	0.812
flux 3	0.6076	0.1078	1.68	0.1078	27.3	0.35	3.136	27.3	0.6594	0.826	1.092	2.1042	1.4798
flux 4	0.9352	0.35	0.812	1.092	0.707	1.0472	0.6832	0.4256	0.532	0.6832	0.6076	0.644	0.7196
flux 5	27.3	1.68	1.358	0.644	0.6076	0.826	0.7	0.0518	0.602	1.4182	0.1078	2.0664	1.0192
flux 6	1.3566	0.532	31.92	0.91	1.3566	3.136	1.3566	2.0664	31.92	0.7196	20.51	1.428	0.707
flux 7	1.134	0.4844	0.959	0.812	0.868	1.204	0.1638	0.707	1.2922	0.9604	0.1638	0.602	0.756
flux 8	1.0976	1.134	0.7	0.9912	0.4256	0.6706	1.2208	2.1042	2.408	1.0472	0.6832	0.7686	20.51
flux 9	0.9604	0.9912	0.4844	0.707	0.6706	0.7	0.6832	31.92	0.9352	1.2922	0.3654	0.532	0.7
flux 10	3.542	0.63	4.06	0.756	5.544	0.9702	1.2068	6.678	4.2322	4.228	8.974	3.766	2.87

Cratère-Sud

CS	29/03/17	30/03/17	31/03/17	01/04/17	02/04/17	03/04/17	04/04/17	05/04/17	06/04/17	07/04/17	08/04/17	09/04/17	10/04/17
flux 0	1.2922	0.63	1.47	2.408	27.3	0.672	1.72	43.33	1.27	31.92	0.658	2.016	0.756
flux 1	0.9352	0.714	0.924	0.826	0.448	20.51	0.742	1.4182	0.7	1.4182	0.9912	0.4844	0.875
flux 2	0.826	1.134	2.016	0.91	1.2208	0.6594	1.3636	2.1042	0.9912	0.756	1.0192	0.532	0.0518
flux 3	1.3566	0.658	0.644	1.204	0.6706	0.63	0.4844	0.35	0.756	2.0664	0.532	0.6706	0.9352
flux 4	1.2208	1.3566	0.154	1.0192	1.4182	0.9912	0.91	0.742	1.4798	0.4256	2.0272	0.714	1.0192
flux 5	0.9912	0.3654	0.714	0.532	2.0272	0.924	0.7686	0.7686	21.7	0.6076	0.3654	0.812	0.714
flux 6	0.1638	0.707	0.756	0.6832	0.63	1.2208	0.714	0.9912	0.6594	0.0518	0.0518	31.92	0.3654
flux 7	0.35	1.778	0.616	0.756	2.0664	0.826	0.0518	1.092	1.134	27.3	2.408	0.756	1.3636
flux 8	32.9	2.0272	0.91	0.4256	0.742	0.707	2.0272	1.3636	43.33	1.428	0.7196	1.4798	0.532
flux 9	0.875	27.3	1.204	0.35	0.4256	1.3636	0.6706	0.6076	1.428	1.3636	0.1078	2.408	21.7
flux 10	4.088	0.7	0.938	0.9114	3.6946	2.8504	1.0136	5.264	7.392	6.72	0.882	4.172	2.828

gridded wind field (u, v, w). This involves four sub-steps: (1) interpolation, (2) smoothing of the analysed field, (3) computation of a vertical velocity field, and (4) minimization of the three-dimensional divergence. Finally, a divergence-minimization procedure is iteratively applied until velocity divergence is smaller than an arbitrarily user defined threshold. The final result of DWM is an approximately null-divergence wind field consistent with the observations (Douglas et al., 1990).

The mass conservation equation for the scaled concentration C may be written in a generalised form as (see Costa et al., 2005; Granieri et al., 2013 and references therein):

$$\frac{\partial C}{\partial t} + U\frac{\partial C}{\partial x} + V\frac{\partial C}{\partial y} + W\frac{\partial C}{\partial z} = \frac{\partial}{\partial t}\left(K_h \frac{\partial C}{\partial x}\right) + \frac{\partial}{\partial y}\left(K_h \frac{\partial C}{\partial y}\right) + \frac{\partial}{\partial z}\left(K_z \frac{\partial C}{\partial z}\right) + Q$$

(2)

where t is time, (U, V, W) are the scaled wind speeds, K_h and K_z are the diagonal scaled diffusion coefficients and Q the source term in the generalised coordinate. To model the passive advection and diffusion of the gas species emitted by the fumaroles at La Soufrière we used the Eulerian DISGAS-2.0, an open-source code for dispersion of dilute gases into the atmosphere (e.g., Costa et al., 2005; Costa and Macedonio, 2016; Granieri et al., 2013, 2017; Pedone et al., 2017). Advective terms in Eq. 2 were discretised according to the second-order Lax–Wendroff

scheme (e.g., Lax and Wendroff, 1960; Ewing and Wang, 2001). The input data in the coupled DWM-DISGAS-2.0 model include topography, terrain roughness, meteorological data, atmospheric stability information, and gas flow rates from the gas sources (for both fumaroles and diffuse degassing). The model yields concentrations at heights selected by the user expressed as values in excess of background gas species levels in the air. It does not account for the chemical reactivity of components and also neglects gas solubility in condensing H_2O droplets.

In this study, the model inputs at sources are the H_2O fluxes, while the outputs are represented by 2D grid maps of H_2O concentrations dispersed over the topography at different timesteps and levels in the atmosphere. The H_2O concentration outputs are then converted in CO_2 and H_2S concentration (ppm) by using the molar ratios CO_2/H_2O and H_2S/H_2O.

Our selected gas/H_2O molar ratios (Allard et al., 2014; Tamburello et al., 2019) were obtained during walking MultiGAS surveys (not permanent station) with short silicone tubes in order to minimize the effect of the water condensation (Moretti et al., 2020a; Jessop et al., 2021).

3.3. Testing the model performance

Mass consistent wind models, such as DWM (Douglas et al., 1990) may produce highly-resolved surface-level wind analyses through surface measurements, which are strongly influenced by the topography,

especially in the immediate vicinity of the station where the topographic reliefs change very sharply. These models are generally more representative during the daytime and in topography simple terrain (Stohl et al., 1997). However, upper-level analyses often provide poor resolutions due to the lack of vertical wind information. This problem is generally overcome by using numerical weather models or radiosondes.

Hence to understand which input data are more appropriate to obtain a reliable wind field, we carried out two tests by using local meteorological data only (Test 1) and ERA5 reanalysis dataset (Copernicus Climate Change Service, 2017; Test 2) in the DWM (Douglas et al., 1990).

Local meteorological data were collected data from the Piton Sanner station operated by OVSG-IPGP and located on the summit dome, at ca. 1447 m (Fig. 1b). This station is equipped with anemometer (05103–03 Campbell), a widevane (05103–03 Campbell) and an atmospheric barometer (PTB101B Campbell).

The meteorological data used in the DWM are the surface temperature and the wind components (Test 1). The same type of data are acquired by ERA5 reanalysis dataset (Test 2). It is worth noting that atmospheric stability information (i.e., the domain-averaged temperature lapse-rate for each hour of the simulation day (K/m) required in DWM is only taken from the ERA5 reanalysis dataset.

To test the impact of uncertainty on topography resolution, we verified whether the fit between simulation results and observations is preserved when using a lower-resolution DEM (25 m; www.earthexplorer.usgs.gov) for the topography (Test 3). In this case, we calculated the wind field by using the data acquired by the local weather station. Finally, to investigate the influence of the computational grid resolution on the model outputs, we reproduced the Test 1 by using a 5 m-resolution computational grid (Test 4).

3.4. Set up of model simulations

The model validation aimed to compare the simulation results carried out under different meteorological conditions (i.e. different wind field data) and grid resolutions with the observations from the permanent OVSG-IPGP stations close to the currently active fumaroles for the periods in which they are available. We chose to simulate the daily cycles (midnight to midnight local time) from 29/03/2017 to 10/04/2017, the only period for which systematic gas concentration measurements are available simultaneously from all the sources (G56, TAS, CS). The observed concentrations were considered in terms of values above the background atmospheric level. The computational domain was extended over an area of 9 km^2 on the volcano and 500 m vertically above the ground (Fig. 1c) and it was discretised by a 200×200 cells grid with a horizontal resolution of 15 m and a vertical grid spacing, finer near the surface (from 1 m) and coarser towards the top (up to 250 m), chosen as a good compromise between the accuracy of outputs and computational costs.

From each simulation, we extracted the CO_2 and H_2S concentration at three tracking points on the summit dome, corresponding to the location of the OVSG-IPGP MultiGAS stations (Fig. 1d, green dots). These points are fixed at 1 m from the ground, so that the observed and simulated concentrations are referred to the same altitude. Since the observations covered 13 days, we provided numerical simulations in two opposite conditions: i) running 11 simulations (each one simulating the entire 13 days of the validation period) varying the daily value of the water vapour flux regardless of each source, in order to catch the natural variability of the gas emission rate shown in the last few years, and ii) running one simulation (simulating the entire 13 days of the validation period) fixing a single water vapour flux for each source. In both cases, the hourly gas concentrations were stored at the tracking points.

We considered the water vapour as the simulated plume component since it prevails in all gas mixtures (Tamburello et al., 2019). To do so, the values of the water vapour fluxes (which are assumed constant on a given simulated day) were randomly sampled from the Empirical

Cumulative Distribution Functions (ECDFs) reported in Appendix B, built on the data available from the literature on this observable (Allard et al., 2014; Tamburello et al., 2019). The ECDFs were assumed representative of the variability in the source fluxes in the selected period, and daily fluxes were assumed independent of each other. In Table 1 we provided the complete dataset of gas fluxes used as input parameters of each fumarole (G56, TAS, CS) for each day of simulation. Thus, in total, 143 different water vapour flux values were sampled for each source (i.e., 13 days times 11 simulations).

Since we focused our attention to the amount of volcanic species in the fumaroles (i.e. H_2S and CO_2), in the post-processing phase, the H_2O concentrations (kg m^{-3}) at the tracking points (Fig. 1d, green dots) were converted into H_2S and CO_2 concentrations (ppm), assuming the same molar ratios estimated for the gases at the source. The molar ratios CO_2/H_2O and H_2S/H_2O used in these conversions were also randomly sampled from the ECDF (Appendix B) built taking into account the 2017 record (Tamburello et al., 2019), again assumed representative of the variability in the molar ratios at the sources.

We note that sources of diffuse soil degassing were not accounted for in the simulations. Allard et al. (2014) estimated the total soil CO_2 flux using a CO_2 accumulation chamber to be was 10% of the fumarolic CO_2 flux in 2006, dropping to 2% in 2012. These estimations were based on measurements made at the Faille de la Ty (FTY) site at the base of the dome (Fig. 1a). Asides steaming ground around the CS fumaroles, no other signs of passive degassing were present on the summit at that time. However, since 2014, a large thermal anomaly has spread over an area of approximately 14,070 m^2 on the summit (north of the chord between NAPE and TAS, Fig. 1a), whereas FTY has remained approximately constant in activity (OVSG-IPGP bulletins, 2006, Jessop et al., 2021).

Soil CO_2 measurements in the area of ground thermal anomalies are currently being performed by the OVSG, and preliminary results suggest a mass flux of around 0.23 kg s^{-1} of CO_2 (OVSG-IPGP Bilan mensuel de l'activité volcanique de la Soufrière de Guadeloupe et de la sismicité régionale, 2020) which is roughly on par with 0.29 kg s^{-1} for the total fumarole CO_2 flux, based on steam flux and H_2O/CO_2 ratios from Giggenbach bottle analyses (OVSG-IPGP Bilan mensuel de l'activité volcanique de la Soufrière de Guadeloupe et de la sismicité régionale, 2006; Moretti et al., 2020a; Jessop et al., 2021). However, given that none of the three permanent MultiGAS stations used for validation in the project are downwind of this site, it is unlikely that diffuse ground emissions would affect the validation tests.

4. Simulation workflow

We developed an automatized workflow which uses Python and Bash scripts to: i) download ERA5 reanalysis data and/or pre-process weather data, (i.e. from a weather station in the domain) and successively process these in the DWM (through a meteorological processor called DIAGNO; Douglas et al., 1990) to obtain the wind field needed by the numerical model; ii) randomly assign the emission rates to the investigated sources on the basis of the ECDFs built from literature data; iii) perform the simulations; iv) post-process the results to obtain contour plots of gas concentration.

The workflow starts defining the input meteorological data. As mentioned above, we defined three configurations for the workflow (Tests 1, 2 and 3). In the first configuration, we used the data collected from the Piton Sanner station (Fig. 1b). These data reproduce accurately the local time-averaged wind field with a 1 h time resolution, but they describe one specific point only (the station) and do not spatially constrain the DWM model. In Test 2, we took into account the data from ERA5 dataset, which covers the Earth on a 30-km grid and resolve the atmosphere using 37 levels from the surface up to a height of 80 km. We first interpolated ERA5 weather data to the location of interest, then we collected wind data for 13 levels up to 500 m above the ground, along with the parameters relative to the stability conditions of the atmosphere. Also in this case the time-step acquisition is 1 h. It is worth

noting that, in all simulations, the information regarding the atmospheric stability needed for the DWM (i.e. the domain-averaged temperature lapse-rate in K/km, specified for 24 h of simulation) derives from the ERA5 dataset. In Appendix A, we provided the hourly averages of wind direction and intensity from both the Piton Sanner station and ERA5 dataset.

To evaluate the wind field over the computational domain, we run the DWM, which uses a terrain-following coordinate system. It needs topography data, average wind on the computational domain, and atmospheric stability information within the scale of the domain (i.e. the temperature gradient in K/m). The wind field was taken to be divergence free, which approximation is generally applicable up to a kilometre above ground level (Dutton and Fichtl, 1969). Furthermore, since terrain-following coordinates were used, this approximation still holds even if ground level varies significantly within the computational domain. The wind field was then linearly interpolated into the computational grid.

The topography of the investigated area is read by DISGAS-2.0 which automatically interpolates the elevations onto the nodes of the computational grid. The topography file specifies ground elevation at a regional scale (i.e. in a region typically equal or larger than the computational domain) by using a structured grid using arbitrary (but constant) grid spacing. The only necessary requirement is that the computational domain must lay within the bounds of the region where topography is specified. The fumaroles were modelled as point sources whose strength (mass flow rate expressed in kg s^{-1}) was specified in the input file.

5. Results

As we are aiming to test the model ability in reproducing the observations from a hazard perspective, we chose daily averages in gas concentration as the simulated quantity to be compared with observations, as it represents the basis for applying a simulator in a probabilistic hazard assessment.
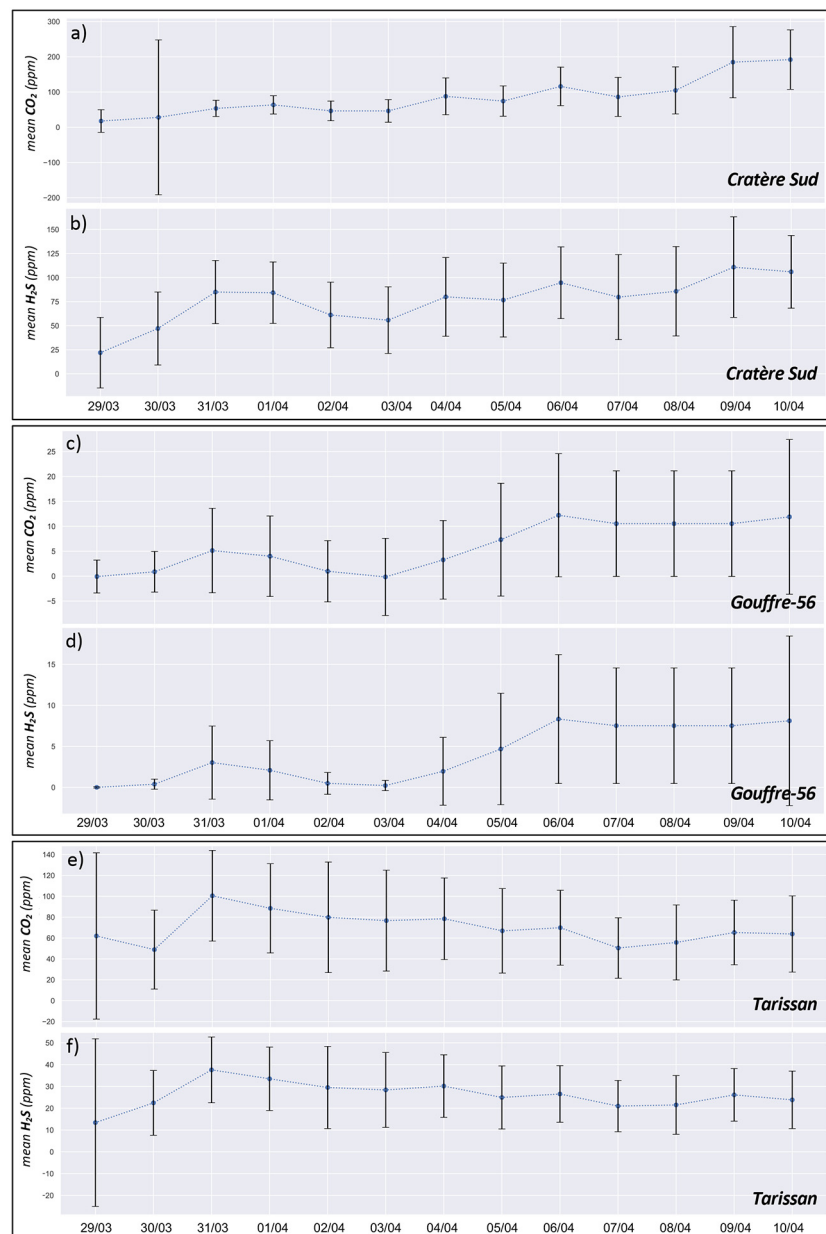

Fig. 2. Daily means of the observed CO_2 and H_2S concentrations (in ppm above the background atmospheric concentration) emitted from CS, G56 and TAS fumaroles, from 29/03/2017 to 10/04/2017. Vertical bars show the standard deviation $\pm 1\sigma$.

In Fig. 2 we reported the daily averages of gas concentration (μ_i) (above the atmospheric background level; ca. 400 ppm for CO_2, and 0 ppm for H_2S) with the associated standard deviation (σi), measured during each day of the investigated period (from 29/03/2017 to 10/04/2017).

Recently, Jessop et al. (2021) compared the steam flux values obtained with different methodologies (airborne thermal camera survey and in situ measurements of temperature and flow rate through temperature probes, Pitot-tube and MultiGAS measurements). MultiGAS retrieved H_2O fluxes (obtained by scaling the CO_2 fluxes with the
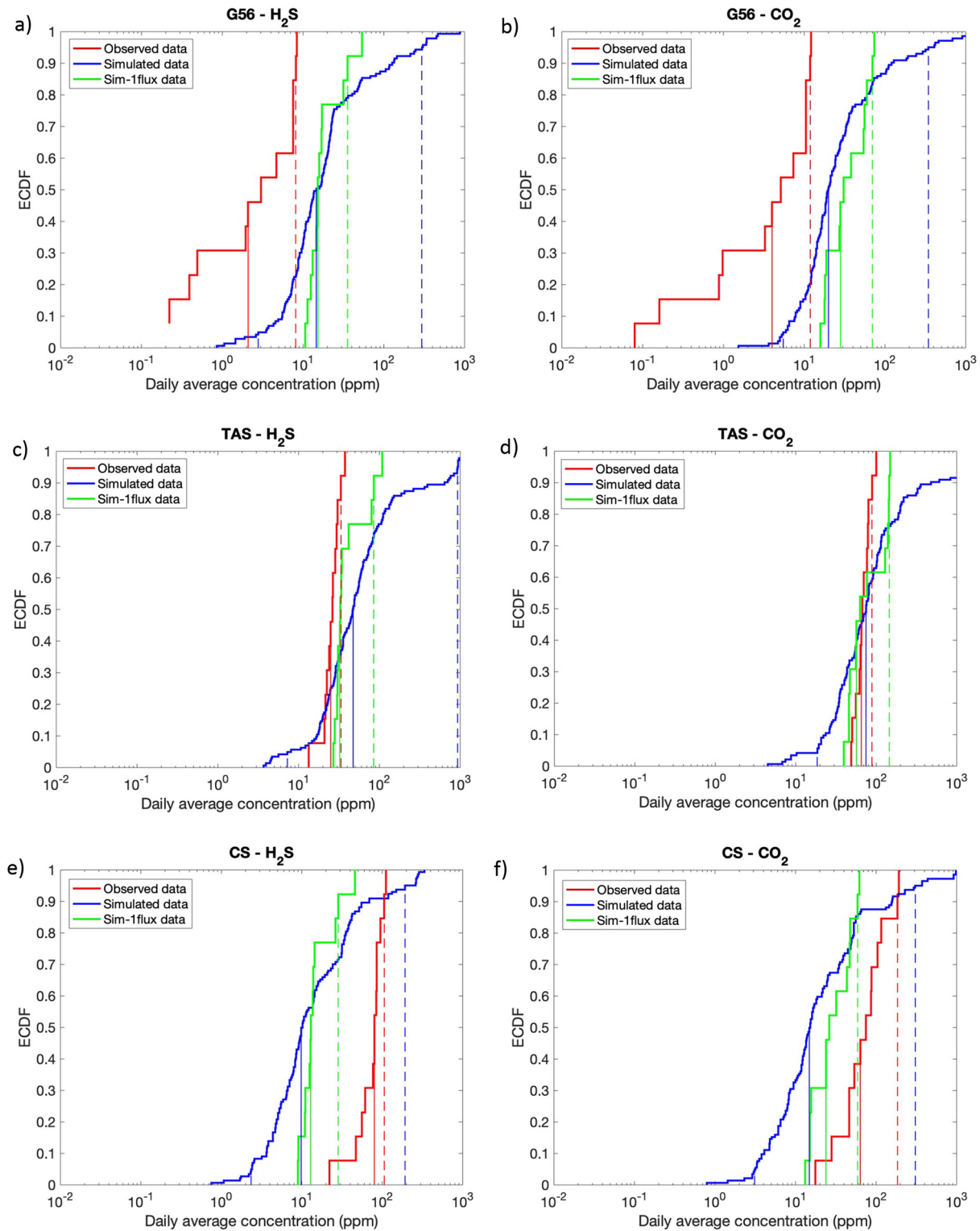
Fig. 3. Results of the model validation taking into account the local meteorological data (Test 1). For each fumarolic source, the Empirical Cumulative Density Functions (ECDFs) of the observed and simulated daily averages of H_2S and CO_2 concentrations are shown for G56 (a-b), TAS (c-d), CS (e-f). The red curve represents the observed data while the blue and green curves are referred to the simulated data obtained by randomly varying the water flux and by setting a fixed flux at source, respectively. The 50° percentile of the ECDFs is represented by the coloured vertical solid lines, while the 5° and 95° percentiles are represented by the dotted vertical lines. The topography is represented by a 5 m resolution DEM. The computational grid has a 15 m resolution.

H_2O/CO_2) can underestimate by ~40% the real steam flux values. Hence, although we applied a 40% correction to account for the condensed water vapour, it is worth noting that the MG-derived steam fluxes have to be considered as minimum estimates.

The results for Tests 1, 2, 3 and 4 are reported in Figs. 3–6, respectively. For each fumarolic source, we provided the ECDFs of the observed and simulated daily averages of H_2S and CO_2 concentrations (G56, Figs. 3-6, panels a-b; TAS: Figs. 3-6, panels c-d; CS: Figs. 3-6, panels
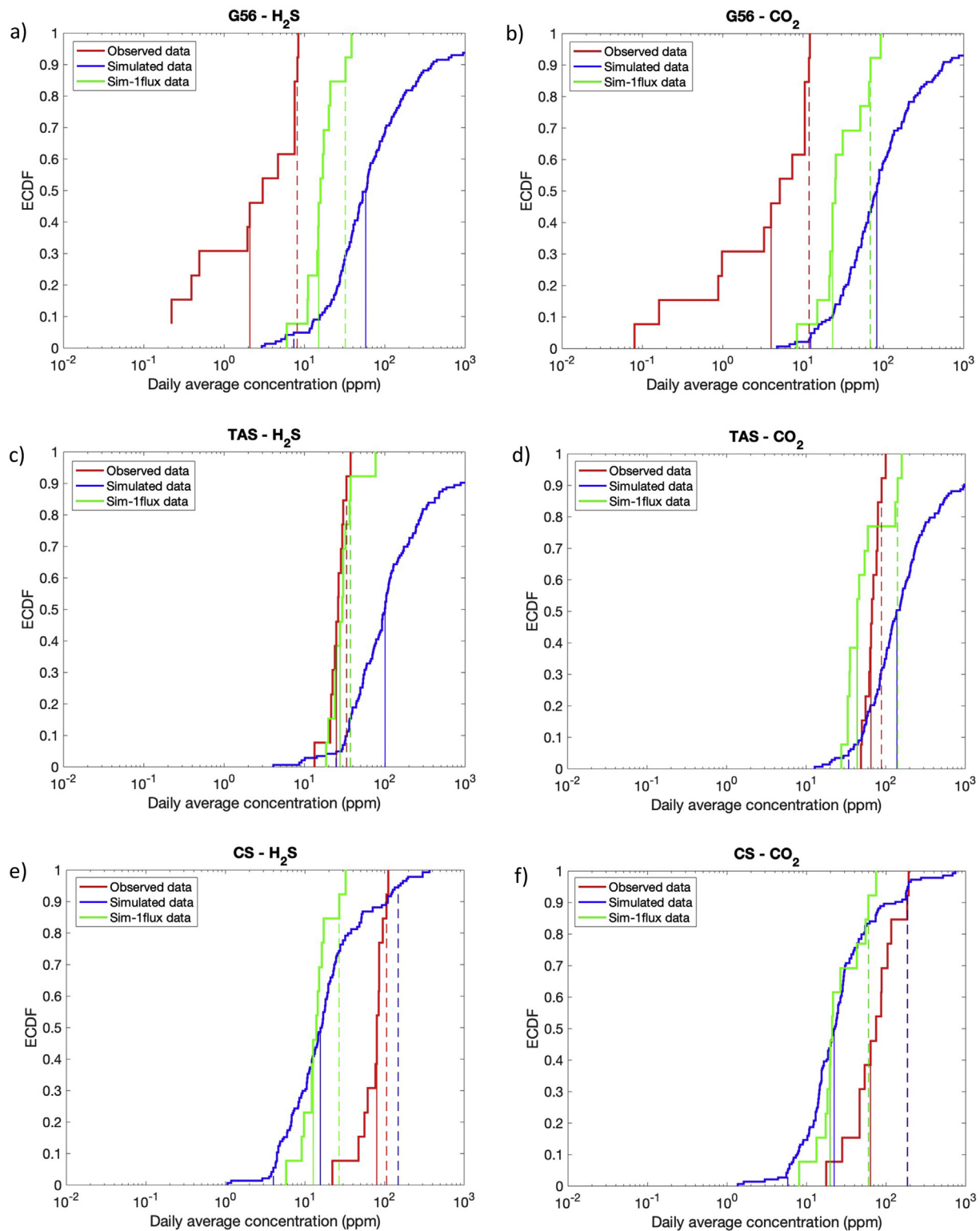
Fig. 4. Results of the model validation taking into account the ERA5 dataset to calculate the wind field (Test 2). For each fumarolic source, the Empirical Cumulative Density Functions (ECDFs) of the observed and simulated daily averages of H_2S and CO_2 concentrations are shown for G56 (a-b), TAS (c-d), CS (e-f). The red curve represents the observed data while the blue and green curves are referred to the simulated data obtained by randomly varying the water flux and by setting a fixed flux at source, respectively. The 50° percentile of the ECDFs is represented by the coloured vertical solid lines, while the 5° and 95° percentiles are represented by the dotted vertical lines. The computational grid has a 15 m resolution.
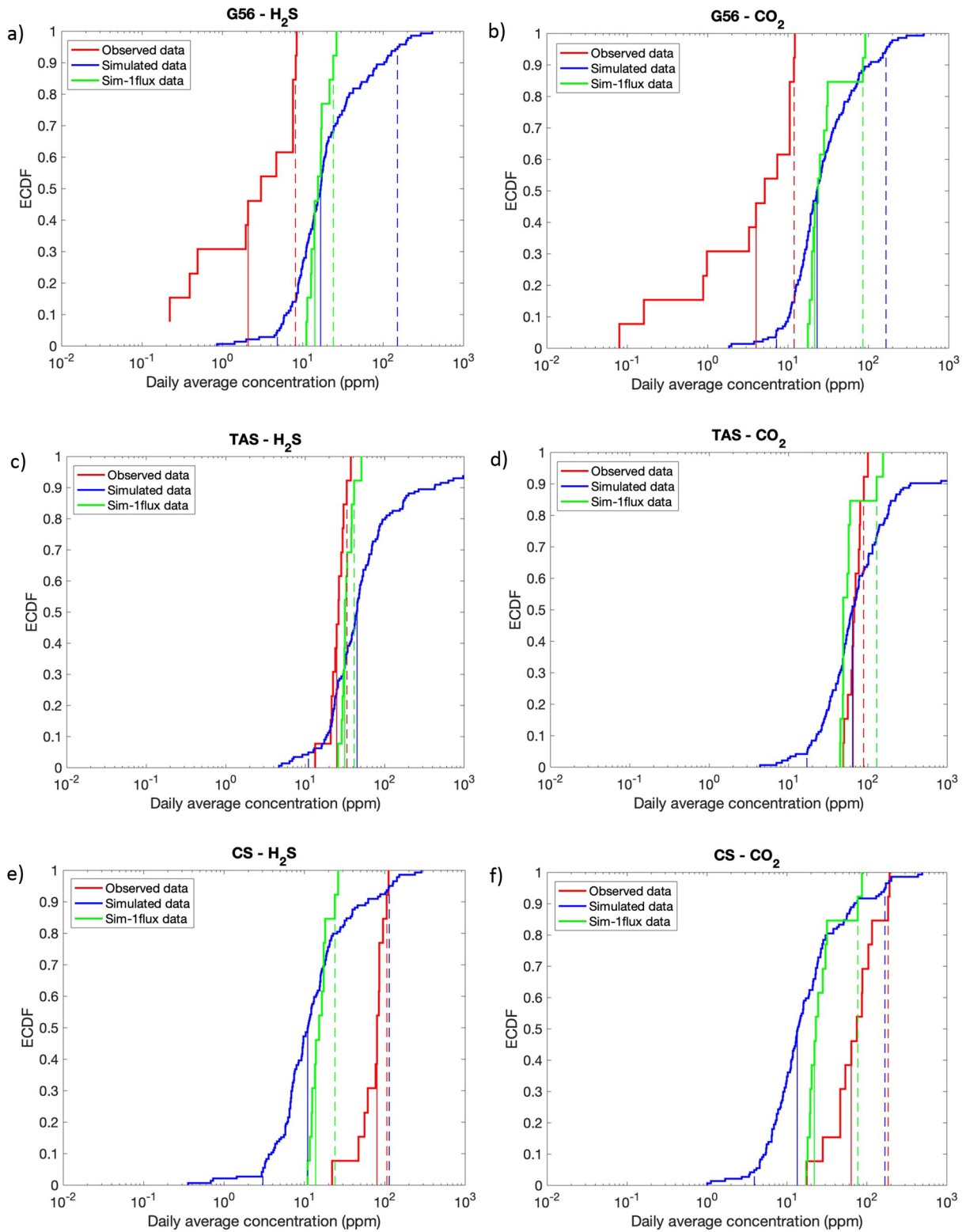
Fig. 5. Results of the model validation using a DEM resolution of 25 m (Test 3), taking into account the local meteorological data to calculate the wind field. For each fumarolic source, the Empirical Cumulative Density Functions (ECDFs) of the simulated and observed daily averages of H_2S and CO_2 concentrations are shown for G56 (a-b), TAS (c-d), CS (e-f). The red curve represents the observed data while the blue and green curves are referred to the simulated data obtained by randomly varying the water flux and by setting a fixed flux at source, respectively. The 50° percentile of the ECDFs is represented by the coloured vertical solid lines, while the 5° and 95° percentiles are represented by the dotted vertical lines. The topography is represented by a 5 m resolution DEM. The computational grid has a 15 m resolution.

e-f). The ECDFs of the simulated concentrations are obtained either by randomly varying the gas fluxes (blue curves) or by using fixed estimates (green curves) at source (Figs. 3-6).

Regarding the simulated data obtained by randomly changing the gas fluxes, for each source we sampled the H_2O water flux 11 times a day from the ECDF in Appendix B. Being the investigation period of 13
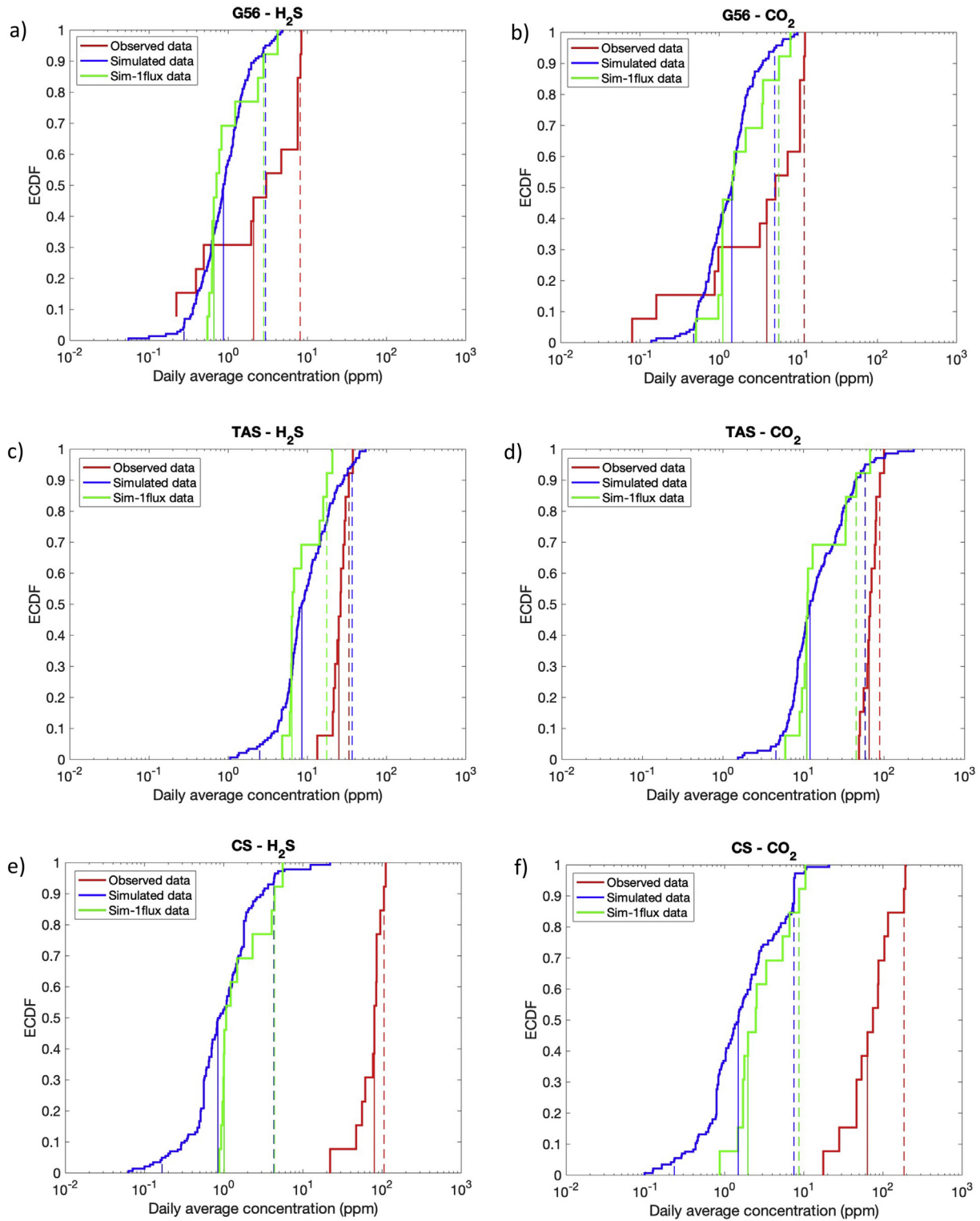

Fig. 6. Results of the model validation obtained by running the Test 1 with a computational grid resolution of 5 m (Test 4). For each fumarolic source, the Empirical Cumulative Density Functions (ECDFs) of the observed and simulated daily averages of H_2S and CO_2 concentrations are shown for G56 (a-b), TAS (c-d), CS (e-f). The red curve represents the observed data while the blue and green curves are referred to the simulated data obtained by randomly varying the water flux and by setting a fixed flux at source, respectively. The 50° percentile of the ECDFs is represented by the coloured vertical solid lines, while the 5° and 95° percentiles are represented by the dotted vertical lines. The topography is represented by a 5 m resolution DEM.

days, to simulate daily variations in gas flux, we ran 11 simulations per day resulting in 143 total simulation runs, which implies a significant amount of computational time as one simulated day required nearly 3 h on a PC with a i5 dual-core processor.

We also provided further numerical simulations by using a fixed flux at each fumarolic source as the most similar to the observed water vapour flux (1.10 kg s^{-1} for G56, 0.93 kg s^{-1} for TAS, and 1.63 kg s^{-1} for CS, considering the estimates in Tamburello et al., 2019 and Jessop et al., 2021) for the entire period of simulation (13 days).

In the following, we describe some general aspects emerged from an overall analysis of the testing procedure. Similarly to ash dispersal models (e.g. Macedonio and Costa, 2012; Macedonio et al., 2016; Selva et al., 2018), the results are indifferent to the selection of the reference input (local or regional) meteorological data: no remarkable differences were observed between Tests 1 and 2 (Figs. 3-4). The wind fields produced by either wind data type were very similar (Appendix A). Hence, the choice of one or another did not impact strongly on our results, implying that either meteorological dataset could be used as input to the DWM. Test 3 showed that a low resolution DEM (25 m) does not affect the model outputs (Fig. 5). Notable differences between the daily averages of observed and simulated concentrations are instead observed in Test 4 (Fig. 6), when the model accounted for a finer computational grid resolution (5 m).

In Tests 1, 2 and 3 we noted that the gas concentration variability shown by the simulated daily averages obtained by randomly varying the water vapour fluxes at source (blue curves) well captured the observed data (red curves) at TAS (Figs. 3–5, panels c-d), but showed marked over estimations at G56 (Figs. 3–5, panels a-b). The simulated daily averages for CS tend to underestimate the observations in all Tests, especially when a higher resolution of computational grid is taken into account (Test 4; Fig. 6e-f).

When looking at the simulated data carried out by using a fixed gas flux at sources (green curves), at TAS we found a very good accordance with the observed daily averages (red curves) in Tests 1–2-3 (Figs. 3–5, panels c-d). In particular, the case of H_2S in Test 2 (Fig. 4c) is emblematic as the observations (red curve) intersect only the tail of the simulated data (blue curve) but they appear perfectly aligned with the simulations obtained with the fixed water flux at source (green curve). This evidence confirms that the selected water flux estimates are robust input data to reproduce the observations, although over and under estimations of about an order of magnitude were observed for G56 and CS, respectively (Figs. 3–5, panels a-b-c-d).

However, different results were shown in Test 4 where the model results for G56 show a better accordance with observations (Fig. 6a-b). Upon inspection of the relative positions of the source and tracking points corresponding to the measurement sites in the computational domain, we ascribed this evidence to the fumarole-station geometry on the computational domain. In particular, G56 source is very close to the top left boundary of a computational cell whilst the tracking point is on the right-hand boundary of the adjacent cell (Fig. 1e). In such a situation, when the plume is advected westward, this configuration may lead to an overestimation of gas concentrations at the tracking point (green dot, Fig. 7a) since the adjacent left-hand cell would record a relatively high concentration due to the presence of the source (red star, Fig. 7a), even if the latter is not at the cell centre. In this case, both cells hosting the source and the station would have very similar concentration values. This is due to how the model is able to solve the real shape of the plume depending on the grid resolution: a low resolution tends to spread the concentration gradients that can locally lead to underestimate in some regions and overestimate in others the simulated concentrations, especially where the observations would have marked gradients. In the case of G56, the observed data showed low gas concentrations since the measurement station was set upwind. This implies that the modelling carried out with a lower resolution grid (15 m) overestimated the observations (Fig. 7a). Once the grid resolution is increased to 5 m, the plume shape is refined and the measurement station does not fall in it
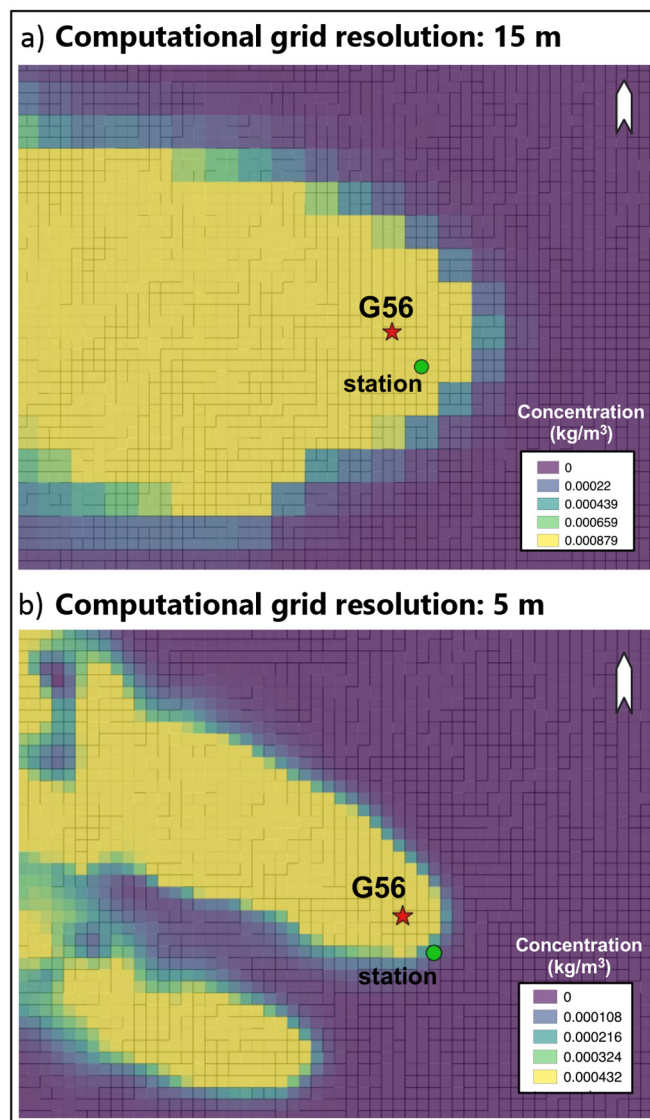

Fig. 7. Plots showing an example of simulated gas dispersion from G56 carried out with 15 m (a) and 5 m (b) resolution of computational grid, under an easterly wind direction. At increasing the resolution, lower gas concentrations are found near the station (green dot, map b). For both cases, the wind field is calculated taking into only account the local meteorological data. The topography is represented by a 5 m resolution DEM.

(Fig. 7b). Unlike G56, the source-station positions of TAS and CS fumaroles provided a worse accordance with observations when the grid resolution is increased at 5 m (Test 4; Fig. 6, panels c-d-e-f). Consequently, the correspondence between simulated data and observations seems to be more satisfactory when using the 15 m grid resolution (Tests 1–2-3; Figs. 3–5).

On the whole, the model results showed an acceptable agreement with the observed data from a hazard point of view. This indicates the potential usefulness of gas dispersion modelling as a promising tool for reproducing the observed fumarolic degassing and for gas hazard assessment purposes. In this regard, taking as reference the model settings of Test 1, we tracked the amount of gas dispersed at 1 m from the ground in a short period of time (from 30/03/2017 to 03/04/2017) outside the dome area (Fig. 8a), providing the average of the overall simulated gas concentrations for a control point located on the SW flank of the volcano (Fig. 1d, yellow dot). The aim of this additional test was to verify if the order of magnitude of the averaged gas concentrations
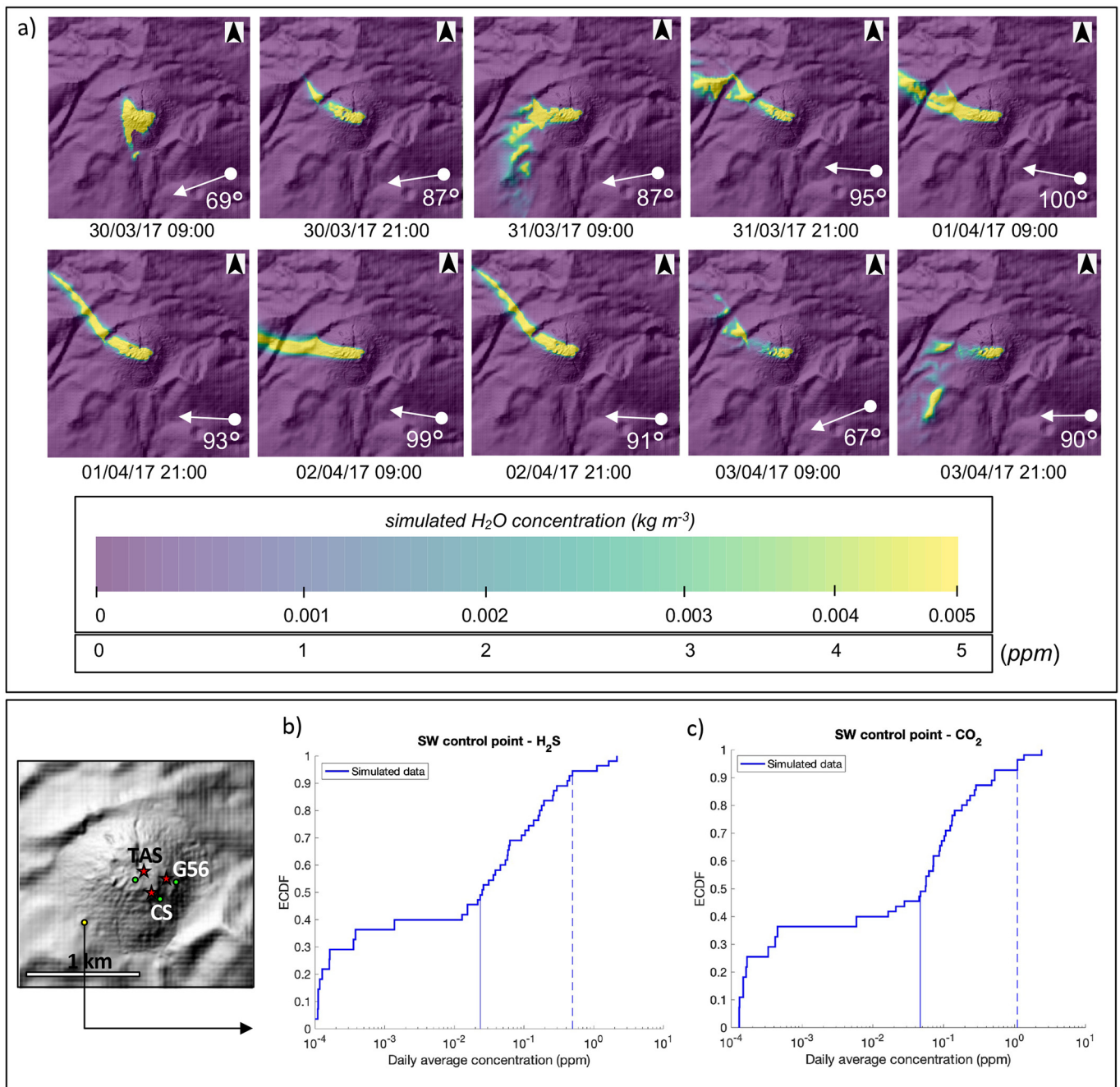
Fig. 8. a) Temporal evolution of the simulated gas dispersion around La Soufrière from 30/03/2017 to 03/04/2017; b) simulated averages of H_2S and CO_2 concentrations calculated above a control point (643,108 E; 1,774,190 N; yellow dot, Fig. 1d) outside the dome area, along the SW flank of the volcano, from 30/03/2017 to 3/04/2017. The wind field was calculated by using the local meteorological data. The topography is represented by a 5 m resolution DEM. The computational grid has a 15 m resolution.

dispersed in few days can potentially be dangerous for people living within few km from La Soufrière. The model results showed that both the daily averages of H_2S and CO_2 concentrations range from 10^{-4} to less than 10 ppm above the background values (Figs. 8b-c) therefore they are not dangerous to health (e.g., World Health Organization and Regional Office for Europe, 2000; Costa et al., 2008; Edmonds et al., 2018 and references therein).

6. Discussion and conclusions

The testing procedure proposed in this work aimed to draw some general best practices to use when dealing with gas hazard quantifications. To do this, we chose La Soufrière de Guadeloupe as case study given the quasi-permanent degassing shown from its last magmatic eruption in 1530 CE. This represents a hazard since the volcano is actively visited by tourists, guides, park operators and the OVSG staff throughout the entire year. These people could be affected by health problems such as sore throat, eye irritation, headache and olfactory paralysis if subjected to a short-medium exposure whilst ascending to the summit. Furthermore, the closest urban agglomerates (i.e., Papaye, Matouba) are located within a few km from the active dome. For these reasons, gas dispersion modelling of the emissions from each site is potentially a very useful tool for quantitative risk assessment, like at many active volcanic-hydrothermal sites

(e.g., Erfurt-Cooper, 2018) where residents and visitors commonly expose themselves to unhealthy levels of toxic gases without adequate understanding of the health risks. In this respect, the choice of a specific modelling tool and its validation represent the very first step for achieving unbiased hazard quantifications.

Here, we showed that modelling using a new implementation of a gas dispersion code (DISGAS-2.0) and varying DEMs and meteorological and field data, is able to capture the order of magnitude and the statistical property of the natural variability displayed by the averages of the observed CO_2 and H_2S concentrations over the entire period of simulation.

Due to lack of simultaneous data from gas sources (i.e., gas flux at specific times, for a period of few days at least) and distal gas concentration measurement points (at hundred of meters to few km away from the source), we could not extend our validation up to a larger spatial scale. This would be desirable in future studies, especially to estimate gas hazard at inhabited areas on the island. Hence, the model outputs shed lights on different aspects to consider for gas hazard purposes in any other volcanic contexts.

Overall, despite the limitations of using the Eulerian approach to reproduce dispersion in the proximity of the gas sources discussed above (i.e., the initial stage of point source emission cannot be treated properly by the Eulerian approach due to its grid nature; Boybeyi and Raman, 1995; Costa et al., 2005) and the limited available meteorological stations (or nodes on a reanalysis grid) within the computational domain leading to a non-optimal setup for the wind field, the performed numerical simulations of Tests 1 and 2 provided a satisfactory representation of the statistical properties of the natural system variability. Considering a limited area of investigation, we showed that meteorological data obtained from local weather stations and reanalysis datasets (as those from ERA5) are capable of reproducing realistic wind fields on a terrain such as around the edifice of La Soufrière de Guadeloupe, as inputs for the gas dispersion modelling.

Moreover, it is well known that the topography can significantly influence plume transport and diffusion (Kaneston Scientific, 1998). In particular, topography and surface roughness can change wind speeds, directions and turbulence characteristics; for example, the presence of significant valleys can restrict horizontal movement and dispersion encouraging the development and persistence of drainage flows (Douglas et al., 1990). Previous applications of DISGAS concerned simple, relatively flat topographies such as calderas (i.e., Solfatara crater, Phlegrean Fields, Italy; Granieri et al., 2013; Pedone et al., 2017; La Fossa crater, Vulcano Island, Italy; Granieri et al., 2017) that lead to a high wind field representativeness (Stohl et al., 1997). In this application, the local topography represents a steep dome of the order of 500 m in diameter and more than 100 m high (Figs. 1c-d). The investigation on the influence of the topography on model results by varying the resolution of the DEM from 5 m (Tests 1–2; Figs. 3-4) to 25 m (Test 3; Fig. 5), revealed that both resolutions well capture the features and the effects of the dome on the meteorological fields.

Looking at each single model output, we noted that the three fumarole-station geometries at La Soufrière dome showed significant differences. Gouffre-56 fumarole is located in a deep fracture right below the eastern edge of the dome and is 3–4 m wide at the surface (Figs. 1c-d). The G56 station has been forcibly located (as best compromise between vicinity to the gas plume and sheltering from the strong winds) few meters from the vent and windward respect to the dominant wind. As consequence, the observed data showed numerous cases of low volcanic gas concentrations, below the resolution of the sensor, that cannot be used for comparison with our simulations. With regard to this, we remark that in this study the G56 gas measurements (maximum daily average for CO_2 is ca.13 ppm, and for H_2S is 8.62; Fig. 2a) were affected by a high uncertainty due to the MultiGAS accuracy of $\pm 2\%$. As explained in Section 4, since the measurement station was set upwind, the observed data showed low gas concentrations, implying that the modelling carried out with

a 15 m-resolution grid overestimated the observations with respect to the 5 m-resolution one.

Tarissan fumarole is a bubbling pond located in a ~ 40 m wide crater at deeply under the dome surface. The TAS station is located ~8 m from the source and downwind with respect to the dominant wind. In this case, the fumarole-station geometry is the most favourable to provide the best accordance between model results and observations in each modelling setup.

Cratèr Sud is a system of three fumaroles (named as north CSN, central CSC and south CSS) located along a north-south oriented fracture in the southern edge of the dome. These fumaroles are ~10 m distant from each other and separated by spurs of rock. For the same logistic problems faced in G56, the station has been installed in the southernmost part of the CS fracture, not exactly downwind the degassing fumaroles. In this light, CS represents the most complex fumarole-station geometry. In Tests 1–2-3 we noted that the underestimations of the simulated data with respect to the observations are balanced by using the 15 m-resolution grid. When the simulations are carried out with the 5 m-resolution, the underestimations are more pronounced (Test 4; Fig. 6e-f) since the model algorithm tends to be numerically less diffusive by using a finer grid resolution.

In general, as the best compromise between accuracy of results and computational time, we found that a 5 m-resolution DEM represents a satisfactory topography for all the modelled source conditions, along with a 15 m-resolution computational grid.

Analysing the results from the modelling, we found that G56 and CS show complex fumarole-station geometries which provide a worse accordance between simulated and observed data. However, we also attempted a first-order inverse approach in order to find out the best input gas flux able to reproduce the observations at G56 and CS sources.

Taking into account the model parameters used in Test 1, we scaled the previous fixed gas fluxes (1.10 kg s^{-1} for G56, and 1.63 kg s^{-1} for CS; Tamburello et al., 2019; Jessop et al., 2021) to a factor representing the ratio between the 50° percentile of simulated and observed gas concentrations. We run additional simulations using new fixed water gas flux of 0.20 and 6.50 kg s^{-1} for G56 and CS, respectively, for the entire investigated period (i.e., 13 days). For G56, the ECDFs resulting from the simulated CO_2 and H_2S concentrations (magenta curves) intersect the observed data (red curves; Fig. 9a-b), indicating that the scaled water gas flux at source provides a satisfactory accordance with observations. For CS, we noted that the ECDFs of the observed data (red curves) are within the ECDFs obtained by using the fixed gas fluxes (green and magenta curves) for both CO_2 and H_2S (Fig. 9e-f). This implies that the best gas flux to use to reproduce the observations would range between 1.63 and 6.50 kg s^{-1}.

It is worth noting that this inverse approach is not necessary for TAS source since the fixed gas flux used in the modelling was previously assessed to have a good accordance with observations (Fig. 9c-d).

As main target, this testing on gas dispersion modelling may be useful to study the prolonged exposure to low concentrations since it could nonetheless affect local population, animal health and agriculture to varying degrees downwind of the volcano and up to a distance of a few km. In this regard, we think that a better quantification of the daily averages of H_2S and CO_2 concentrations outside the dome area (similar to that reported in Fig. 8) should be carried out over a larger area and for a longer period of time. In particular, for CO_2 the long-time exposure limit (LTEL) is set to 5000 ppm (time weighted average, TWA) for working-age-people in good health exposed to the gas for 8 h/d in 5 days per week, while for H_2S, the LTEL is set to 5 ppm (TWA) for a 8 h/d for 5 days per week (World Health Organization and Regional Office for Europe, 2000).

At La Soufrière, given the increase in fumarolic activity recorded since February 2018 and extension of the fumarolic area, an intensification of phenomena in the future cannot be excluded (Moretti et al., 2020a; Jessop et al., 2021), since the hydrothermal system is recharging towards a P-T condition corresponding to that just prior to the 1976–77
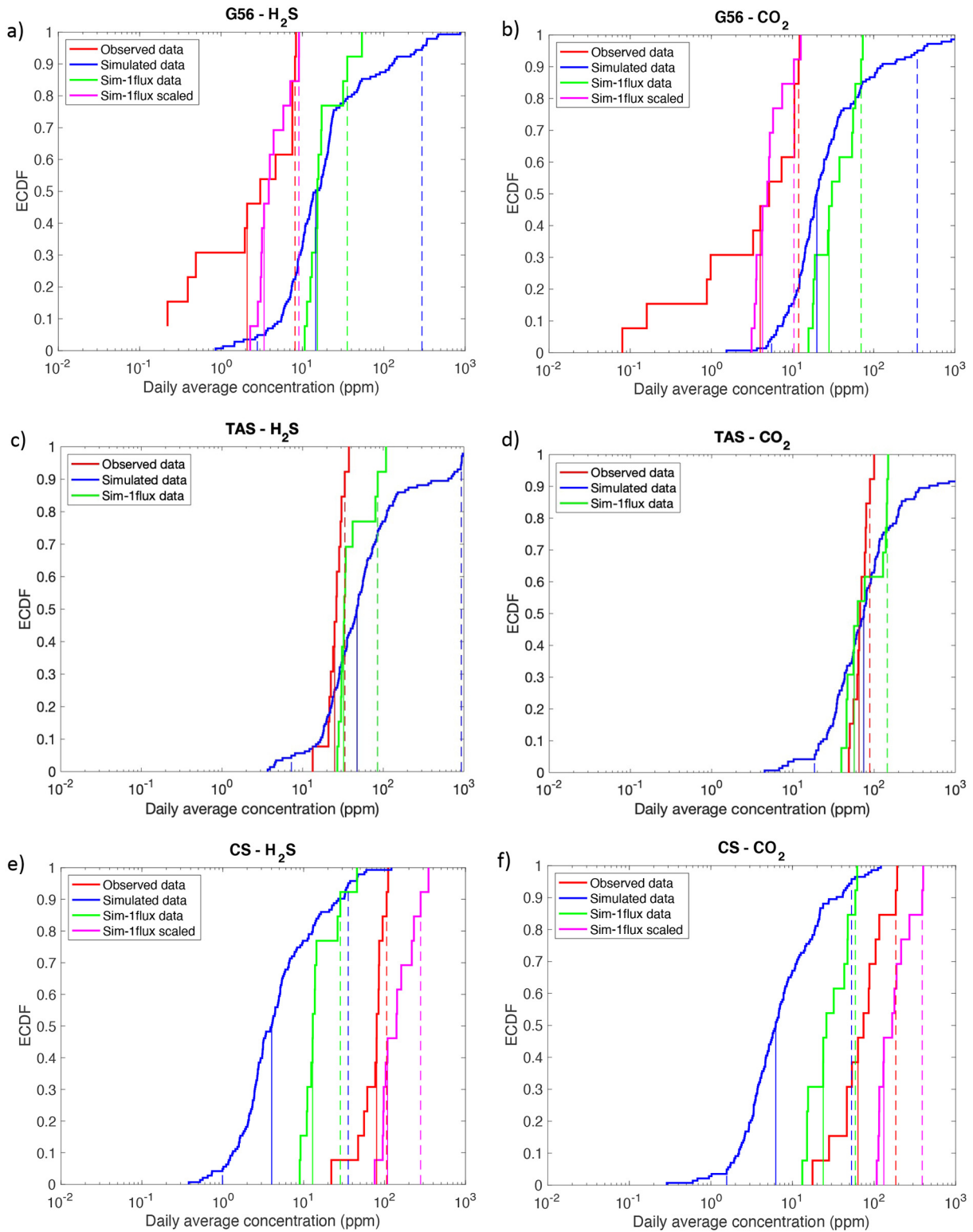
Fig. 9. Results from Test 1 showing the Empirical Cumulative Density Functions (ECDFs) of the observed and simulated daily averages of H_2S and CO_2 concentrations for G56 (a-b), TAS (c-d), CS (e-f). The ECDF of the observed and simulated data obtained by randomly varying the water flux are represented by red and blue curves, respectively. The ECDFs obtained by setting a fixed flux at source from reference literature (1.10 kg s^{-1} for G56, 0.93 kg s^{-1} for TAS, and 1.63 kg s^{-1} for CS; Tamburello et al., 2019; Jessop et al., 2021), are represented by the green curves. Additional ECDFs (magenta curves) are provided by using fixed gas flux which is scaled to the ratio between the 50° percentile of the observed and simulated data (red and green vertical solid lines) for G56 (a-b; 0.20 kg s^{-1}) and CS (e-f; 6.50 kg s^{-1}). For all ECDFs, the 5° and 95° percentiles are represented by the dotted vertical lines. The topography is represented by a 5 m resolution DEM. The computational grid has a 15 m resolution.

unrest phase. In addition to this, in case of a potential more concentrated gas dispersion due to increased activity of the volcanic system in the future, the plume condition could turn, depending on gas temperature, into conditions of negative or positive buoyancy for which DISGAS-2.0 is no longer suitable for modelling the phenomena. At present, the proposed modelling approach is appropriate for producing gas hazard maps for La Soufrière.

In conclusion, in this study we investigated the modelling requirements to correctly reproduce the statistics of observations. We found that an appropriate setting of the computational grid resolution is fundamental in gas hazard, while it is relatively less important the type of DEM resolution (e.g., Tierz et al., 2017) and the type of meteorological data used. Notably, this is fundamental to produce an unbiased hazard quantification. Although it is very common to use a model to fit a given set of observations, or to assess hazard, we highlight that it is still quite uncommon to study the ability of models to reproduce the statistics in the data of interest, that should actually be the first logical step to be taken when applying a simulator to assess hazard.

Declaration of Competing Interest

The authors declare that they have no known competing financial interests or personal relationships that could have appeared to influence the work reported in this paper.

Acknowledgements

Appendix A. Supplementary data

Supplementary data to this article can be found online at https://doi.org/10.1016/j.jvolgeores.2021.107312.

References

Aiuppa, A., Federico, C., Giudice, G., Gurrieri, S., 2005. Chemical mapping of a fumarolic field: la Fossa crater, Vulcano Island (Aeolian Islands, Italy). Geophys. Res. Lett. 32 (13).

Aiuppa, A., Moretti, R., Federico, C., Giudice, G., Gurrieri, S., Liuzzo, Papale P., Shonohara, H., Valenza, M., 2007. Forecasting Etna eruptions by real-time observation of volcanic gas composition. Geology 35 (12), 1115–1118.

Aiuppa, A., Bertagnini, A., Métrich, N., Moretti, R., Di Muro, A., Liuzzo, M., Tamburello, G., 2010. A model of degassing for Stromboli volcano. Earth Planet. Sci. Lett. 295 (1–2), 195–204.

Aiuppa, A., Lo, Coco E., Liuzzo, M., Giudice, G., Giuffrida, G., Moretti, R., 2016. Terminal Strombolian activity at Etna's central craters during summer 2012: The most CO2-rich volcanic gas recorded at Mount Etna. Geochem. J. 50.

Aiuppa, A., Bitetto, M., Francofonte, V., Velasquez, G., Parra, C.B., Giudice, G., Liuzzo, M., Moretti, R., Moussallam, Y., Peters, N., Tamburello, G., Valderrama, O.A., Curtis, A., 2017a. A CO2 gas precursor to the March 2015 Villarrica volcano eruption. Geochem. Geophys. Geosyst. 18 (6), 2120–2132.

Aiuppa, A., Fischer, T.P., Plank, T., Robidoux, P., Di Napoli, R., 2017b. Along-arc, inter-arc and arc-to-arc variations in volcanic gas CO2/ST ratios reveal dual source of carbon in arc volcanism. Earth Sci. Rev. 168, 24–47.

Allard, P., Aiuppa, A., Beauducel, F., Gaudin, D., Di Napoli, R., Calabrese, S., Parello, P., Crispi, F., Hammouya, G., Tamburello, G., 2014. Steam and gas emission rate from La

Soufrire volcano, Guadeloupe (Lesser Antilles): implications for the magmatic supply during degassing unrest. Chem. Geol. 384, 76–93.

Andres, R.J., Kasgnoc, A.D., 1998. A time-averaged inventory of subaerial volcanic sulfur emissions. J. Geophys. Res.-Atmos. 103 (D19), 25251–25261.

Boichu, M., Villemant, B., Boudon, G., 2008. A model for episodic degassing of an andesitic magma intrusion. J. Geoph. Res Solid Earth 113 (B7).

Boichu, M., Villemant, B., Boudon, G., 2011. Degassing at La Soufrière de Guadeloupe volcano (Lesser Antilles) since the last eruptive crisis in 1975–77: result of a shallow magma intrusion? J. Volcanol. Geotherm. Res. 203 (3–4), 102–112.

Boudon, G., Komorowski, J.C., Villemant, B., Semet, M.P., 2008. A new scenario for the last magmatic eruption of La Soufrière of Guadeloupe (Lesser Antilles) in 1530 AD evidence from stratigraphy radiocarbon dating and magmatic evolution of erupted products. J. Volcanol. Geotherm. Res. 178 (3), 474–490.

Boybeyi, Z., Raman, S., 1995. Simulation of elevated long-range plume transport using a mesoscale meteorological model. Atmos. Environ. 29 (16), 2099–2111.

Brombach, T., Hunziker, J.C., Chiodini, G., Cardellini, C., Marini, L., 2001. Soil diffuse degassing and thermal energy fluxes from the southern Lakki plain, Nisyros (Greece). Geophys. Res. Lett. 28 (1), 69–72.

Brothelande, E., Finizola, A., Peltier, A., Delcher, E., Komorowski, J.C., Di Gangi, F., Legendre, Y., 2014. Fluid circulation pattern inside La Soufrière volcano (Guadeloupe) inferred from combined electrical resistivity tomography, self-potential, soil temperature and diffuse degassing measurements. J. Volcanol. Geotherm. Res. 288, 105–122.

Chiodini, G., Frondini, F., Cardellini, C., Granieri, D., Marini, L., Ventura, G., 2001. CO2 degassing and energy release at Solfatara volcano, Campi Flegrei, Italy. J. Geophys. Res. Solid Earth 106 (B8), 16213–16221.

Cortis, A., Oldenburg, C.M., 2009. Short-range atmospheric dispersion of carbon dioxide. Bound.-Layer Meteorol. 133 (1), 17–34.

Costa, A., Macedonio, G., 2016. DISGAS: A Model for Passive DISpersion of GAS. Rapporti tecnici INGV. 332. Istituto Nazionale Di Geofisica e Vulcanologia, Italy (2039e7941).

Costa, A., Macedonio, G., Chiodini, G., 2005. Numerical model of gas dispersion emitted from volcanic sources. Ann. Geophys. 48 (4–5).

Costa, A., Chiodini, G., Granieri, D., Folch, A., Hankin, R.K.S., Caliro, S., Cardellini, C., Avino, R., 2008. A shallow layer model for heavy gas dispersion from natural sources: application and hazard assessment at Caldara di Manziana, Italy. Geochem. Geophys. Geosyst. 9 (Q03002).

Costa, A., Folch, A., Macedonio, G., 2013. Density-driven transport in the umbrella region of volcanic clouds: Implications for tephra dispersion models. Geophys. Res. Lett. 40 (18), 4823–4827.

Dabbert, W., Miller, E., 2000. Uncertainty, ensembles and air quality dispersion modeling: applications and challenges. Atmos. Environ. 24, 4667–4673.

de Moor, J.M., Aiuppa, A., Avard, G., Wehrmann, H., Dunbar, N., Muller, C., Tamburello, G., Liuzzo, M., Moretti, R., Conde, V., Galle, B., 2016. Turmoil at Turrialba Volcano (Costa Rica): Degassing and eruptive processes inferred from high-frequency gas monitoring. J. Geophys. Res. Solid Earth 121 (8), 5761–5775.

Di Napoli, R., Aiuppa, A., Bellomo, S., Brusca, L., D'Alessandro, W., Candela, E., Longo, M., Pecoraino, G., Valenza, M., 2009. A model for Ischia hydrothermal system: evidences from the chemistry of thermal groundwaters. J. Volcanol. Geotherm. Res. 186 (3–4), 133–159.

Douglas, S.G., Kessler, R.C., Carr, E.L., 1990. User's guide for the Urban Airshed Model. Volume 3. User's manual for the Diagnostic Wind Model (No. PB-91-131243/XAB). Systems Applications, Inc., San Rafael, CA (USA).

Dutton, J.A., Fichtl, G.H., 1969. Approximate equations of motion for gases and liquids. J. Atmos. Sci. 26 (2), 241–254.

Edmonds, M., Grattan, J., Michnowicz, S., 2018. Volcanic gas: Silent killers. Observing the Volcano World: Volcano Crisis Communication. Springer, Cham, pp. 65–84.

Erfurt-Cooper, P., 2018. Active hydrothermal features as tourist attractions. Observing the Volcano World: Volcano Crisis Communication. Springer, Cham, pp. 85–105.

Ewing, R., Wang, H., 2001. A summary of numerical methods for time-dependent advection-dominated partial differential equations. J. Comput. Appl. Math. 128, 423–445.

Feuillard, M., Allegre, C.J., Brandeis, G., Gaulon, R., Le Mouel, J.L., Mercier, J.C., Semet, M.P., 1983. The 1975–1977 crisis of la Soufrière de Guadeloupe (FWI): a still-born magmatic eruption. J. Volcanol. Geotherm. Res. 16 (3–4), 317–334.

Folch, A., Costa, A., Hankin, R., 2009. Twodee-2: a shallow layer model for dense gas dispersion on complex topography. Comput. Geosci. 35 (3), 667–674.

Folch, A., Barcons, J., Kozono, T., Costa, A., 2017. High-resolution modeling of atmospheric dispersion of dense gas using TWODEE-2.1: application to the 1986 Lake Nyos limnic eruption. Nat. Hazards Earth Syst. Sci. 17, 1–19. https://doi.org/10.5194/nhess-17-861-2017.

Giggenbach, W.F., 1996. Chemical composition of volcanic gases. Monitoring and Mitigation of Volcano Hazards. Springer, Berlin, Heidelberg, pp. 221–256.

Granieri, D., Costa, A., Macedonio, G., Bisson, M., Chiodini, G., 2013. Carbon dioxide in the urban area of Naples: Contribution and effects of the volcanic source. J. Volcanol. Geotherm. Res. 260, 52–61.

Granieri, D., Vita, F., Inguaggiato, S., 2017. Volcanogenic SO2, a natural pollutant: Measurements, modeling and hazard assessment at Vulcano Island (Aeolian Archipelago, Italy). Environ. Pollut. 231, 219–228.

Grattan, J.P., Pyatt, F.B., 1999. Volcanic eruptions dry fogs and the European palaeoenvironmental record: localised phenomena or hemispheric impacts? Glob. Planet. Chang. 21 (1–3), 173–179.

Hankin, R.K.S., Britter, R.E., 1999. Twodee: the Health and Safety Laboratory's shallow layer model for heavy gas dispersion part 3: Experimental validation (Thorney Island). J. Hazard. Mater. 66 (3), 239–261.

Harris, A.J.L., Delle Donne, D., Dehn, J., Ripepe, M., Worden, A.K., 2013. Volcanic plume and bomb field masses from thermal infrared camera imagery. Earth Planet. Sci. Lett. 365, 77–85.

Hernández, P.A., Pérez, N.M., Fridriksson, T., Egbert, J., Ilyinskaya, E., Thárhallsson, A., ... Padrón, E., 2012. Diffuse volcanic degassing and thermal energy release from Hengill volcanic system, Iceland. Bull. Volcanol. 74 (10), 2435–2448.

Hofmann, D.J., 1987. Perturbations to the global atmosphere associated with the El Chichon volcanic eruption of 1982. Rev. Geophys. 25 (4), 743–759.

Jessop, D.E., Moune, S., Moretti, R., Gibert, D., Komorowski, J.-C., Robert, V., Heap, M.J., Bosson, A., Bonifacie, M., Deroussi, S., Dessert, C., Rosas-Carbajal, M., Lemarchand, A., Burtin, A., 2021. A multi-decadal view of the heat and mass budget of a volcano in unrest: La Soufrière de Guadeloupe (French West Indies). Bull. Volcanol. 83, 16. https://doi.org/10.1007/s00445-021-01439-2.

Komorowski, J.C, et al., 2001. L'activité éruptive et non-éruptive de la Soufrière de Guadeloupe: problèmes et implications de la phénoménologie et des signaux actuellement enregistrés. (French). Eruptive and non-eruptive activity from la Soufrière of Guadeloupe: problems and implications posed by the current phenomenology and monitoring signals. Workshop on Volcanic Hazards - Lesser Antilles Volcanoes: From Processes to Signals. PNRN (CNRS), INSU, BRGM, CEA, CEMAGREF, CNES, IRD, pp. 18–19.

Komorowski, J.C., Boudon, G., Semet, M., Beauducel, F., Anténor-Habazac, C., Sand Hammouya, G., 2005. Guadeloupe. Volcanic hazard atlas of the Lesser Antilles: Guadeloupe. Volcanic Hazard Atlas of the Lesser Antilles. pp. 65–102.

Lax, P.D., Wendroff, B., 1960. Systems of conservative laws. Commun. Pure Appl. Math. 13, 217–237.

Le Gonidec, Y., Rosas-Carbajal, M., de Bremond d'Ars, J., Carlus, B., Ianigro, J.C., Kergosien, B., Gibert, D., 2019. Abrupt changes of hydrothermal activity in a lava dome detected by combined seismic and muon monitoring. Sci. Rep. 9 (1), 1–9.

Legendre, Y., 2012. Reconstruction fine de l'histoire éruptive et scénarii éruptifs à la Soufrière de Guadeloupe: vers un modèle intégré de fonctionnement du volcan (Doctoral dissertation, Paris 7).

Lewellen, W.S., Sykes, R.I., 1989. Meteorological data needs for modeling air quality uncertainties. J. Atmosp. Oceanic Techn. 6 (5), 759–768.

Macedonio, G., Costa, A., 2002. Finite element modeling of gas dispersion in the atmosphere. Proceedings of the Arezzo Seminar in Fluids Geochemistry. Pacini, Ospedaletto (Pisa), Italy, pp. 147–159.

Macedonio, G., Costa, A., 2012. Brief communication. Rain effect on the load of tephra deposits. Nat. Hazards Earth Syst. Sci. 12 (4), 1229–1233.

Macedonio, G., Costa, A., Scollo, S., Neri, A., 2016. Effects of eruption source parameter variation and meteorological dataset on tephra fallout hazard assessment: example from Vesuvius (Italy). J. Appl. Volcanol. 5 (1), 1–19.

McGonigle, A.J.S., Oppenheimer, C., Galle, B., Mather, T.A., Pyle, D.M., 2002. Walking traverse and scanning DOAS measurements of volcanic gas emission rates. Geophys. Res. Lett. 29 (20) (46–1).

Moretti, R., Stefansson, A., 2020. Volcanic and geothermal redox engines. Elements Int. Mag. Min. Geochem. Petrol. 16 (3), 179–184.

Moretti, R., Arienzo, I., Civetta, L., Orsi, G., Papale, P., 2013. Multiple magma degassing sources at an explosive volcano. Earth Planet. Sci. Lett. 367, 95–104.

Moretti, R., Troise, C., Sarno, F., De Natale, G., 2018. Caldera unrest driven by CO_2-induced drying of the deep hydrothermal system. Sci. Rep. 8 (1), 1–11.

Moretti, R., Komorowski, J.C., Ucciani, G., Moune, S., Jessop, D.E., de Chabalier, J.B., Beauducel, F., Bonifacie, M., Burtin, A., Vallè, M., Deroussi, S., Robert, V., Gibert, D., Didier, T., Kitou, T., Feuillet, N., Allard, P., Tamburello, G., Shreve, T., Saurel, J.M., Lemarchand, A., Rosas-Carbajal, M., Agrinier, P., Le Friant, A., Chaudisson, M., 2020a. The 2018 unrest phase at La Soufrière of Guadeloupe (French West Indies) andesitic volcano: Scrutiny of a failed but prodromal phreatic eruption. J. Volcanol. Geotherm. Res. 106769.

Moretti, R., Moune, S., Robert, V., Jessop, D.E., Didier, T., Bonifacie, M., Komorowski, J.C., 2020b. Intercomparison of geochemical techniques at La Soufrière de Guadeloupe (FWI) volcano: their advantages and their limits over a long-standing unrest. Ital. J. Geosci. 139, 398–412. https://doi.org/10.3301/IJG.2020.13.

Oppenheimer, C., 2002. Limited global change due to the largest known Quaternary eruption, Toba≈ 74 kyr BP? Quat. Sci. Rev. 21 (14–15), 1593–1609.

Oppenheimer, C., Pyle, D.M., Barclay, J., 2003. Volcanic Degassing. Geological Society of London.

Oppenheimer, C., Moretti, R., Kyle, P.R., Eschenbacher, A., Lowenstern, J.B., Hervig, R.L., Dunbar, N.W., 2011. Mantle to surface degassing of alkalic magmas at Erebus volcano, Antarctica. Earth Planet. Sci. Lett. 306 (3–4), 261–271.

OVSG-IPGP Bilan mensuel de l'activité volcanique de la Soufrière de Guadeloupe et de la sismicité régionale, 1999–2013; 2006; 2018. Observatoire volcanologique et sismologique de Guadeloupe – Institute de Physique du Globe de Paris.

Parker, D.E., Wilson, H., Jones, P.D., Christy, J.R., Folland, C.K., 1996. The impact of Mount Pinatubo on world-wide temperatures. Int. J. Climatol. 16 (5), 487–497.

Pedone, M., Granieri, D., Moretti, R., Fedele, A., Troise, C., Somma, R., De Natale, G., 2017. Improved quantification of CO_2 emission at Campi Flegrei by combined Lagrangian Stochastic and Eulerian dispersion modelling. Atmos. Environ. 170, 1–11.

Pichavant, M., Le Gall, N., Scaillet, B., 2018. Gases as precursor signals: experimental simulations, new concepts and models of magma degassing. Volcanic Unrest. Springer, Cham, pp. 139–154.

Rissmann, C., Christenson, B., Werner, C., Leybourne, M., Cole, J., Gravley, D., 2012. Surface heat flow and CO_2 emissions within the Ohaaki hydrothermal field, Taupo Volcanic Zone, New Zealand. Appl. Geochem. 27 (1), 223–239.

Rosas-Carbajal, M., Komorowski, J.C., Nicollin, F., Gibert, D., 2016. Volcano electrical tomography unveils edifice collapse hazard linked to hydrothermal system structure and dynamics. Sci. Rep. 6, 29899.

Rougier, J., Beven, K.J., 2013. Model and data limitations: the sources and implications of epistemic uncertainty. Risk Uncert. Assess. Nat. Haz. 40.

Ruzié, L., Moreira, M., Crispi, O., 2012. Noble gas isotopes in hydrothermal volcanic fluids of La Soufrière volcano, Guadeloupe, Lesser Antilles arc. Chem. Geol. 304, 158–165.

Scientific, Kanestone, 1998. Dispersion of Fine Particulate Pollution within and near Busway Tunnels. Report from Kanestone Scientific to Connell Wagner Pty Ltd.

Scire, J.S., Strimaitis, D.G., Yamartino, R.J., 2000. A user's guide for the CALPUFF dispersion model. 521. Earth Tech. Inc, pp. 1–521.

Self, S., 1845. 2006. The effects and consequences of very large explosive volcanic eruptions. Philosophical transactions of the Royal Society a: Mathematical. Phys. Eng. Sci. 364, 2073–2097.

Selva, J., Costa, A., De Natale, G., Di Vito, M.A., Isaia, R., Macedonio, G., 2018. Sensitivity test and ensemble hazard assessment for tephra fallout at Campi Flegrei, Italy. J. Volcanol. Geotherm. Res. 351, 1–28. https://doi.org/10.1016/j.jvolgeores.2017.11.024.

Shinohara, H., 2005. A new technique to estimate volcanic gas composition: plume measurements with a portable multi-sensor system. J. Volcanol. Geotherm. Res. 143 (4), 319–333.

Sigurdsson, H., Houghton, B., McNutt, S., Rymer, H., Stix, J., 2015. The Encyclopedia of Volcanoes. Elsevier.

Stein, A.F., Draxler, R.R., Rolph, G.D., Stunder, B.J., Cohen, M.D., Ngan, F., 2015. NOAA's HYSPLIT atmospheric transport and dispersion modeling system. Bull. Amer. Met. Soc. 96 (12), 2059–2077.

Stohl, A., Baumann, K., Wotawa, G., Langer, M., Neininger, B., Piringer, M., Formayer, H., 1997. Diagnostic downscaling of large-scale wind fields to compute local-scale trajectories. J. Appl. Met. 36 (7), 931–942.

Symonds, R.B., 1994. Volcanic-gas studies: Methods, results, and applications, in Volatiles in magma. Rev. Mineral. 30, 1–66.

Tamburello, G., Moune, S., Allard, P., Venugopal, S., Robert, V., Rosas-Carbajal, M., Deroussi, Gaëtan-Thierry Kitou, Didier, T., Komorowski, J.C., Beauducel, F., De Chabalier, J.B., Le Marchand, A., Le Friant, A., Bonifacie, M., Dessert, C., Moretti, R., 2019. Spatio-Temporal Relationships between Fumarolic Activity, Hydrothermal Fluid Circulation and Geophysical Signals at an Arc Volcano in Degassing Unrest: La Soufrière de Guadeloupe (French West Indies). Geosciences 9 (11), 480.

Tierz, P., Sandri, L, Costa, A., Zaccarelli, L., Di Vito, M.A., Sulpizio, R., Marzocchi, W., 2016. Suitability of energy cone for probabilistic volcanic hazard assessment: Validation tests at Somma-Vesuvius and Campi Flegrei (Italy). Bull. Volcanol. 78, 79–92. https://doi.org/10.1007/s00445-016-1073-9.

Tierz, P., Sandri, L, Costa, A., Sulpizio, R., Zaccarelli, L., Di Vito, M.A., Marzocchi, W., 2017. Uncertainty Assessment of Pyroclastic Density Currents at Mount Vesuvius (Italy) Simulated Through the Energy Cone Model. In: Riley, K., Webley, P., Thompson, M. (Eds.), "Natural Hazard Uncertainty Assessment: Modeling and Decision Support". Geophysical Monograph, First edition 223. American Geophysical Union, John Wiley & Sons, Inc.

Tortini, R., van Manen, S.M., Parkes, B.R.B., Carn, S.A., 2017. The impact of persistent volcanic degassing on vegetation: a case study at Turrialba volcano. Costa Rica. Int. J. Applied Earth Obs. Geoinform. 59, 92–103.

Venkatram, A., 1981. Model predictability with reference to concentrations associated with point sources. Atmos. Environ. 15 (9), 1517–1522.

Villemant, B., Hammouya, G., Michel, A., Semet, M.P., Komorowski, J.C., Boudon, G., Cheminée, J.L., 2005. The memory of volcanic waters: shallow magma degassing revealed by halogen monitoring in thermal springs of La Soufrière volcano (Guadeloupe, Lesser Antilles). Earth Planet. Sci. Lett. 237 (3–4), 710–728.

Villemant, B., Komorowski, J.C., Dessert, C., Michel, A., Crispi, O., Hammouya, G., De Chabalier, J.B., 2014. Evidence for a new shallow magma intrusion at La Soufrière of Guadeloupe (Lesser Antilles): insights from long-term geochemical monitoring of halogen-rich hydrothermal fluids. J. Volcanol. Geotherm. Res. 285, 247–277.

World Health Organization, Regional Office for Europe, 2000. Air Quality Guidelines for Europe. 2nd ed. WHO Regional Office for Europe, Copenhagen https://apps.who.int/iris/handle/10665/107335.

Zlotnicki, J., Boudon, G., Le Mouël, J.L., 1992. The volcanic activity of La Soufrière of Guadeloupe (Lesser Antilles): structural and tectonic implications. J. Volcanol. Geotherm. Res. 49 (1–2), 91–104. https://doi.org/10.1016/0377-0273(92)90006-Y.